arXiv:1701.07397v1 [astro-ph.GA] 25 Jan 2017

Comparing binary systems from rotating parent gas structures with different total masses

Guillermo Arreaga-García[1]

Departamento de Investigación en Física, Universidad de Sonora, Apdo. Postal 14740, C.P. 83000, Hermosillo, Sonora, Mexico.

ABSTRACT

In this paper we continue the investigation reported by Arreaga (2016) concerning the morphology of binary configurations obtained via the collapse of rotating parent gas structures with total masses in the range of M_T= 1 to 5 $M_\odot$. Here we extend the mass range and consider the collapse of two uniform gas clumps of M_T= 50 and 400 $M_\odot$, so that they also rotates rigidly in such a way that its approximate virial parameter takes the values of 0.5, 1.5, and 2.5 and their collapse is induced initially by implementing an azimuthal mass perturbation. To assess the effects of the total mass of the parent gas structure on the nature of the resulting binary configurations, we also consider the collapse of two cores of M_T= 1 and 5 $M_\odot$. We calculate the collapse of all these parent gas structures using three values of the ratio of thermal energy to potential energy and for two values of the mass perturbation amplitude. We next calculate the binary separations, masses and integral properties of the binary fragments and present them in terms of the total mass of the parent structure. For most of our models, we finally calculate the β extreme value, so that a model with a slightly higher β value would no longer collapse.

Subject headings: –stars: formation, –physical processes: gravitational collapse, hydrodynamics, – methods: numerical

1. Introduction

Stars are formed in gravitationally collapsed clouds made of molecular hydrogen gas. These gas clouds appear to be composed of many well-defined gas substructures, so that these assembled clouds can be very large and massive. Thus, all gas structures have been characterized according to Bergin and Tafalla (2007) by means of their size and mass. For instance, a gas clump is a gas structure with mass and size in the range of 50-500 $M_\odot$ and 0.3-3 pc, while for a gas core these values are in the range of 0.5-5 $M_\odot$ and 0.03-0.2 pc.

Numerical simulations of the collapse of a rotating, self-gravitating, isolated cloud cores, began to be performed many years ago; see Bodenheimer et al. (1980), Boden (2011). One of the classic models of binary formation is based on the collapse of a rotating spherical core of 1 $M_\odot$, in which an azimuthal symmetric mass perturbation was initially implemented such that a binary system was formed by prompt fragmentation; see the so-called "standard isothermal test case" calculated by Boss and Bodenheimer (1979), Boss (1991), Truelove et al (1998), Klein et al. (1999), Boss et al. (2000), and Kitsionas and Whitworth (2002), among others.

It has always been very important to determine whether or not a gas structure is stable against gravitational collapse. As early as two decades ago, theorists proposed collapse and fragmentation criteria by constructing configuration diagrams, the axes of which are usually the ratio of thermal energy to potential energy, denoted by α, versus the ratio of rotational energy to gravitational energy, denoted by β; see for instance Miyama (1984), Hachisu and Heriguchi (1984), Hachisu and Heriguchi (1985), and Tsuribe et al. (1999).

It must be emphasized that numerical simulations are still necessary to conclusively show the final configuration obtained from the collapse of a particular model of gas structure, as all these α versus β configuration diagrams mentioned are, above all, mostly indicative, due to the fact that the parameter space that determines the final simulation outcome is very large.

We mention that the role played by the total mass of the parent core on the collapse results has been considered for a long time ago. For instance, Tscharnuter (1975) chose initial conditions in order to study the collapse of a cloud of M=60 $M_\odot$ and compared it to the collapse of three models of 1 $M_\odot$. Rozyczka et al (1980) investigated the collapse and fragmentation in four cloud models, of which the first three are for 1 $M_\odot$ and the last one is a model of a very massive uniform cloud of 5000 $M_\odot$. Furthermore, Boss (1986) studied in depth the collapse of rotating, uniform non-isothermal clouds by considering a four dimensional parameter space composed by α, β, T and the total mass M. The upper limit of M was 2 $M_\odot$ while the range of α and β varied within 0.01-0.50 and 0-0.33, respectively. He found four different types of configurations and noted that as the mass M decreased, cloud fragmentation is less favored.

More recently, Arreaga (2016) reported numerical simulations focusing on only one type of binary configuration, consisting of a well-defined pair of mass condensations that approach each other, achieve rotational speed, swing past each other, and finally separate to form the desired binary system, in which the mass condensations orbit around one another at the end of the simulation. A schematic diagram was also presented in which this particular binary configuration can be located among others. Similar configurations were also obtained

by Hennebelle et al. (2004) by increasing the external pressure on a rotating core. The configuration that interested Arreaga (2016) corresponds to the disk-bar type fragmentation studied by Matsumoto and Hanawa (2003) and Tsuribe (2002).

The schematic diagram reported by Arreaga (2016) was constructed with the total mass of the parent core M_T as the vertical axis in the range of 0.75 to 5 $M_\odot$, versus the dimensionless ratio of rotational energy to gravitational energy β, as the horizontal axis in the range of 0.1 to 0.21. The dimensionless ratio of thermal energy to potential energy, α, was kept fixed for all simulations. It was also noted that the increase in the total mass of the parent core diminished the formation of the desired binary configuration and instead favored the formation of a single central mass condensation surrounded by a disk as the final result.

Observationally, much effort has been put forth for many years in order to determine some physical property that could be useful in deciding whether or not a particular gas structure will collapse. Particularly, the virial parameter, denoted here by α_{vir}, has recently been measured in order to characterize the dynamical state of gas structures. For instance, Kauffmann at al. (2013) recently compiled a catalog of 1325 molecular gas clouds of very different sizes, including estimates of their virial parameters.

There exists a critical virial parameter, denoted here by α_{vir}^{crit}, which comes from a stability study in which perturbations both in pressure and density gradients were considered; it has been mathematically determined that $\alpha_{vir}^{crit} \approx 2$. The common belief in the recent past has been that most gas structures have $\alpha_{vir} > \alpha_{vir}^{crit}$, so that either they do not collapse or will even be diffused into the interstellar medium. It is important to note that Kauffmann at al. (2013) recently observed low values of α_{vir} for regions of high-mass star formation; that is, these gas structures have $\alpha_{vir} < \alpha_{vir}^{crit}$, so they are expected to collapse.

The virial parameter is defined as the ratio of virial mass M_{vir} to the total mass M_T of a gas structure, so that in the case of a spherical model of radius R, it is given by $\alpha_{vir} = \frac{5\,\sigma_v\,R}{G\,M_T}$, where σ_v is the velocity dispersion and G is the Newton's gravitational constant. It should be noted that the velocity dispersion entering in the calculation of α_{vir} includes both the thermal and the non-thermal velocity components.

When the velocity distribution of a particular model of a gas structure is considered to be composed only of a thermal component, it is possible to relate the α_{vir} to the β ratio by means of $\alpha_{vir} = f\,2\beta$, where f is a form factor, which is empirically included to take into account modifications for non-homogeneous and non-spherical gas distributions.

As it seems that the dimensionless critical virial parameter, which separates the gas clouds that collapse from those that do not, is close to 2, we here prepare initial conditions of the SPH particles to have a rigidly rotating gas structure, such that its β is given by 0.1,

0.3, and 0.48. A possible approximation would be that of using the average velocity $< v >$ of the particle distribution instead of the σ_v. Thus, for a numerical simulation, we would have a virial parameter approximated by $\alpha_{vir} = \frac{5 < v >^2 R}{G M_T}$. So that the values of β given above will correspond to simulations with their approximated α_{vir} values given by 0.5, 1.5, and 2.5, respectively.

Thus, the question raised by the virial parameter in the observational field, of finding where is the transition between the cores that collapse to those that do not, in this paper we translated this question to the numerical simulations field, so that we here locate those models that are near to the non-collapsing regime, such that we call them "the last collapsing configuration". As expected, the occurrence of this last collapsing configuration depends on initial values of α and β and on the total mass of the parent structure.

With regard to the theoretical aspect, we mention that self-similar solutions for the collapse of isothermal spheres were first obtained by Larson (1969) and Penston (1969), and later by Shu (1977). Hunter (1977) performed a detailed mathematical analysis of the collapse problem and re-discovered previous solutions and also obtained new solutions. Other self-similar solutions were also found for the collapse of adiabatic spheres, in which a polytropic equation of state was assumed. All these solutions provide an accurate description of the early collapse stage, which mostly proceeds isothermally, as the gas is optically thin to its own radiation. A radial density profile was obtained from these self-similar solutions. In the case of a rotating collapse with pressure, Tohline (1981) was able to get also the mathematical expression of a radial density profile by using an approach based on the virial theorem. The physical parameters of the parent core are included in the density profile, so that it can be simply scaled for a different set of parameters of a second parent core.

Motivated by the work of Arreaga (2016) mentioned above, in this paper we want to study the formation of binary systems via the collapse of a more massive gas structure; thus, we carry out a fully three-dimensional set of numerical hydrodynamical simulations aimed to model the gravitational collapse of a $M_T \approx 50$ and 400 $M_\odot$ clumps, by using the SPH particle technique, such that a finite number of SPH particles is used to sample the entire gas structure. The formation of two antipode mass seeds during the early collapse stage of the clumps is here enforced by implementing a mass perturbation with the same mathematical structure of the density perturbation successfully used in the classic collapse calculation of Boss et al. (2000) for an isothermal one solar mass core.

When the peak density of the collapsing core is high enough, the central region of the core become opaque to its own radiation; thus the isothermal regime breaks down so that an adiabatic regime begins. In our case, this transition is taken into account by using the barotropic equation of state, first proposed by Boss et al. (2000), which is characterized by

a critical density.

Now, the value of this critical density depends on how much mass surrounds and obscures the central region of the core. In general, it is expected that the more massive the parent cores are, the critical density at which the obscuration occurs may be lower. Strictly speaking, this would imply to change the value of the critical density of the barotropic equation of state in our suite of simulations.

In this paper, we were able to follow the collapse of the clumps up to three orders of magnitude in density within this adiabatic regime, where there are no scaling solutions known, out of which new solutions can be simply scaled from the initial mass of the parent core, as can be done in the isothermal collapse. Because of this, the treatment of this advanced collapse stage must be investigated by means of numerical simulations. As expected, for the first collapse stage, no significance differences in the collapse of a higher mass structure are seen. However, as we will see later, the influence of a higher mass parent structure on the collapse get manifested only in the non-isothermal collapse stage; see Sterzik et al. (2003).

In this paper we re-simulate two core models of 1 and 5 $M_\odot$ with β also given by 0.1, 0.3, and 0.48, respectively. These models are similar but not identical to those already reported by Arreaga (2016). We consider here all those collapse models with values of α given by 0.1, 0.2, and 0.3, in order to make a comparison of our results with those of Riaz et al (2014), who studied the thermal sensitivity of binary formation via the collapse of cores. To complement the qualitative study of binary configurations that we carry out in the first part of this paper, we next present a quantitative analysis of some of the resulting binary configurations, including the calculation of the binary separation and masses of the fragments of some particular binary configurations, and we present them in terms of the total mass of the parent structure.

It should be mentioned that we have not considered here the collapse of a more massive gas structure, such as a gas cloud with mass and size of the order of 10^3-10^4 $M_\odot$ and 2-15 pc. This is due to the fact that it has been suggested by several authors that the observed masses and core separations in regions of high-mass star formation cannot be explained by invoking only fragmentation via gravitational instability; see Liu et al (2015) among others. Thus, the formation process of very massive dense cores in high-mass star formation regions needs other mechanisms to be taken into account other than that of thermal fragmentation (also called Jeans fragmentation), for instance, turbulent fragmentation or magneto-hydrodynamical induced fragmentation.

However, for both the cores and the intermediate mass clumps, such as those considered in this paper, it is expected that only thermal fragmentation is relevant to explain their

fragmentation properties; see Palau et al (2014), Palau et al (2015) and Busquet et al. (2016).

We finally mention that the collapse of cores to model isolated or binary star formation is an active field of research, for example, the evolution of rotating cloud cores including turbulent velocity initial distributions has been investigated by many authors; see for instance: Bate et al. (2002), Bate et al. (2003), Delgado-Donante et al. (2004), Delgado-Donante et al. (2004), Bate et al. (2005) and Goodwin et al. (2007). Collapse calculations of an isothermal cloud core rotating in a uniform magnetic field have been presented, among others, by Price and Bate (2007), Hennebelle and Teyssier (2008), Machida et al (2008) and Boss and Keiser (2013).

2. The physical state of the parent gas structures

All the parent gas structures considered in this paper are uniform spheres, which are rigidly rotating around the z axis with an angular velocity Ω, so the initial velocity of the $i-th$ SPH particle is given by $(-\Omega\, y_i, \Omega\, x_i, 0)$.

The time needed for a test particle to reach the center of a gas sphere, when gravity is the only force acting on it, is defined as the free fall time t_{ff}, and it is given by $t_{ff} \approx \sqrt{\frac{3\,\pi}{32\,G\,\rho_0}}$, where ρ_0 is the average density. We will use ρ_0 and t_{ff} to normalize the figures that appear in the coming sections.

Following Bodenheimer et al. (2000), the dynamical state of a general gas structure is usually characterized by the values of the dimensionless ratios α and β, which are given by

$$\begin{aligned} \alpha &\equiv \frac{E_{therm}}{|E_{grav}|} \\ \beta &\equiv \frac{E_{rot}}{|E_{grav}|} \end{aligned} \tag{1}$$

For a spherical model of a gas structure of total mass M_T, the total gravitational potential energy is approximated by $< E_{grav} > \approx -\frac{3}{5}\,\frac{G\,M_T^2}{R}$, where R is the sphere radius. The average total thermal energy $< E_{therm} >$ (kinetic plus potential interaction terms of the molecules) is $< E_{therm} > \approx \frac{3}{2}\mathcal{N}\,k\,T = \frac{3}{2}M_T\,c_0^2$, where k is the Boltzmann constant, T is the equilibrium temperature, $\mathcal{N}$ is the total number of molecules in the gas, and c_0 is the speed of sound. The rotational energy of the clump is approximately given by $E_{rot} = \frac{1}{2}\,I\,\Omega^2 = \frac{1}{2}\,\frac{J^2}{I} \approx \frac{1}{5}\,M_T\,R^2\,\Omega^2$, where $I \approx \frac{2}{5}\,M_T\,R^2$ is the moment of inertia and $J = I\,\Omega_0$ is the total angular momentum.

If we consider that the velocity dispersion σ_v of a gas structure is directly related only to the thermal velocity component, then $\sigma_v = \sqrt{\frac{k\,T_{kin}}{17\,m_H}}$ where m_H is the molecular mass of the

main gas component and T_{kin} is the kinetic temperature. In this case, an approximation to be used in this paper would be using the average velocity $< v >$ of the simulation particles instead of the σ_v. Thus, we would have a virial parameter approximated by $\alpha_{vir} = \frac{5 < v >^2 R}{G M_T}$.

In this paper, we have carefully selected the values of c_0 and Ω, so the energy ratios obtained by considering all the simulation particles of an initial configuration (the snapshot zero of a simulation) are initially given by a pairs of values taken from the following sets:

$$\begin{aligned} \alpha &\equiv 0.3, 0.2, 0.1 \\ \beta &\equiv 0.1, 0.3, 0.48 \end{aligned} \tag{2}$$

so that the corresponding values of the virial parameter for all our models are approximately given, respectively, by

$$\alpha_{vir} \equiv 0.5, 1.5, 2.5 \tag{3}$$

2.1. The cores

We will consider the gravitational collapse of two cores: the first is a variant of the so-called "standard isothermal test case," which was first calculated by Boss and Bodenheimer (1979) and later calculated by Burkert and Bodenheimer (1993) and Bate and Burkert (1997); the main outcome of this classic model was a protostellar binary system. In this paper, the core radius is R=4.99 $\times 10^{16}$ cm $\equiv$ 0.016 pc and its mass is M_T=1 $M_\odot$. Thus, the average density and the corresponding free fall time of this core are ρ_0 =3.8 $\times 10^{-18}$ g cm^{-3} and t_{ff} $\approx$1.0 $\times 10^{12}$ s $\equiv$ 34077 yr, respectively.

The radius and mass of the second core are R=6.16 $\times 10^{17}$ cm $\equiv$0.2 pc and M_T=5 $M_\odot$, respectively. This core has an average density of ρ_0 =1.0 $\times 10^{-20}$ g cm^{-3} and a t_{ff} $\approx$2.0 $\times 10^{13}$ s $\equiv$ 660997 yr, respectively.

Despite the size and mass differences of these gas structures, both of them are still cores, as defined statistically by Bergin and Tafalla (2007).

2.2. The clumps

The first clump structure considered in this paper has a radius and mass given by R=0.3 pc $\equiv$ 9.24 $\times 10^{17}$ cm and M_T=50 $M_\odot$, respectively. Its average density is given by ϱ_1 =3.0 $\times 10^{-20}$ g cm^{-3}.

The radius and mass of the second clump are given by R=1 pc $\equiv$ 3.08 $\times 10^{18}$ cm and M_T=400 $M_\odot$, respectively. Its average density is ϱ_2 =6.5 $\times 10^{-21}$ g cm^{-3} and its corresponding free fall time is $t_{ff} \approx 2.6 \times 10^{13}$ s $\equiv$826 247 yr.

We emphasize that the radius and mass of the clumps have been changed with respect to those of the cores. In spite of this, it is still possible to make a comparison of the collapse results, as the focus of this paper is to study the effects of changing the values of α and β on the collapse of different parent gas structures. Besides, if we had kept unchanged some physical property of the clump structures, so that we had used the core radius, while the total parent mass is different to that of the cores, then the resulting clump structure would be un-physical, in the statistical sense defined by Bergin and Tafalla (2007).

2.3. The mass perturbation

For every SPH particle i of a simulation with total number of particles N_p, that is, i=1..N_p, the particle mass is given by $m_0 = \frac{M_T}{N_p}$; then we implement a mass perturbation of the type

$$m_i = m_0 + m_0 * a \cos(m \phi_i) \tag{4}$$

where the perturbation amplitude is set to the values of a=0.1 and a=0.25; the mode is fixed to m=2 and ϕ is the azimuthal spherical coordinate.

This mass perturbation scheme was successfully applied in many papers on collapse; see for instance Arreaga et al. (2007), Arreaga et al. (2008), Arreaga and Klapp (2010), and notably Springel (2005), when the Gadget2 code was proven, among other tests, with the calculation of the isothermal collapse, where the unequal mass particles method was validated.

2.4. Resolution

Truelove et al. (1997) demonstrated the need of fulfill appropriate spatial resolution requirements in order to avoid the occurrence of artificial fragmentation in a collapse simulation.

Following Bate and Burkert (1997), the smallest mass that a SPH calculation can resolve, m_r, is given by $m_r \approx 2\, N_{neigh}\, M_J$ where N_{neigh} is the number of neighboring particles included in the SPH kernel and M_J is the spherical Jeans mass M_J, which is defined by

$$M_J \equiv \frac{4}{3}\pi\ \rho \left(\frac{\lambda_J}{2}\right)^3 = \frac{\pi^{\frac{5}{2}}}{6}\frac{c^3}{\sqrt{G^3\,\rho_m}}\ . \tag{5}$$

where λ_J is Jeans wavelength and ρ_m is the peak density reached in a simulation. Therefore, the smallest mass particle m_p in our simulations must at least be such that $\frac{m_p}{m_r} < 1$.

Let us assume that $N_{neigh} = 40$, ρ_m=1.0 $\times 10^{-11}$ g cm^{-3} and that the sound speed c varies within the values 10 369 and 17 868 cm s^{-1}, which correspond to runs with α=0.1 and 0.3 of the 1 M$_\odot$ model, respectively. In this case, the m_r is within 3.0 $\times 10^{27}$ and 1.5 $\times 10^{28}$ g. In the simulations of a 1 M$_\odot$ core, we used N$_p$=2 000 000 of SPH particles, so that m_p is $m_p = 9.9 \times 10^{26}$ g, and then we have that the ratio of masses is m_p/m_r 0.06 and 0.3. Therefore The number of particles is high enough to fulfill the resolution requirements described by Truelove et al. (1997).

For the 5 M$_\odot$ core, the particle mass is m_p=4.9 $\times 10^{27}$ g while the sound speed varies within 9500.0 and 12400.0 cm s^{-1}, so that by using again N$_p$=2 000 000 of SPH particles, the ratios m_p/m_r are appropriate up to peak densities smaller than ρ_m=5.0 $\times 10^{-12}$.

For the 50 M$_\odot$ clump, we used 12 000 000 of SPH particles, so the particle mass is $m_p = 8.2 \times 10^{27}$ g. In this case, the sound speed varies within 17 497 and 29 576 cm s^{-1}, and for a peak density of 1.0 $\times 10^{11}$, m_r are 0.5 and 0.1, respectively.

For the 400 M$_\odot$ clump, a very large number of particles is needed for the simulations to fulfill the resolution requirements. Because computational limitations, we could not achieve the desired resolution and despite of this, we evolved these simulations using only 2 million of SPH particles; for this lack of reliability, we consider them useful only for comparison with the lower mass simulations.

2.5. The barotropic equation of state

In order to ensure the change in the thermodynamic regime from isothermal to adiabatic, we here implement the barotropic equation of state proposed by Boss et al. (2000):

$$p = c_0^2 \rho \left[1 + \left(\frac{\rho}{\rho_{crit}}\right)^{\gamma-1}\right] \tag{6}$$

where γ=5/3 and c$_0$ is the sound speed. The critical density ρ_{crit} has only been given here the value $\rho_{crit} = 5.0 \times 10^{-14}$ g cm^{-3}. As we will show in the following sections, in the simulations considered in this paper, the average peak density increases up to 3 orders of

magnitude within the adiabatic regime.

2.6. Evolution Code

To follow the gravitational collapse of our models, in this paper we use the fully parallelized particle-based code Gadget2, which is based on the tree-PM method for computing the gravitational forces and on the standard SPH method for solving the Euler equations of hydrodynamics; see Springel (2005) and also Springel at al. (2001). The Gadget2 code has implemented a Monaghan-Balsara form for the artificial viscosity; see Monaghan and Gingold (1983) and Balsara (1995). The strength of the viscosity is regulated by setting the parameter $\alpha_\nu = 0.75$ and $\beta_\nu = \frac{1}{2} \times \alpha_v$; see Equations 11 and 14 in Springel (2005). We have fixed the Courant factor to 0.1.

2.7. The initial setup

Herein we used a radial mesh with spherical geometry, such that a set of concentric shells was created and populated with SPH particles by means of a Monte Carlo scheme to set the initial particle configuration.

Thus, all the SPH particles of each simulation, were located randomly in all the available surfaces of each spherical shell. The total mass in each shell is kept constant, so that the global density of the gas structure is also constant. In order to have a constant density distribution in a local sense, we next applied a radial perturbation to all the particles of a given shell such that any particle could be randomly displaced radially outward or inward, but preventing a perturbed particle from reaching another shell; see section 2.1 of Arreaga (2016).

2.8. The collapse models

In Table 1 we summarize the models considered in this paper and the main configurations obtained. Column 1 shows the number of the model; column 3 shows the total mass of the parent structure; column 4 shows the value of the mass perturbation amplitude, defined by Eq.4; column 5 and 6 show the values of the dimensionless ratios α and β, respectively; column 7 shows the type of configuration obtained and column 8 shows the number of the

figure and panel, in which the solution configuration is shown[1].

We now emphasize five types of solution configurations that appear frequently, which may be termed as follows: (i) a face-to-face configuration, characterized by the presence of two fragments located one in front of the other, so that the connecting filament has been entirely accreted; (ii) a connecting filament configuration, in which the filament still plays a relevant role as a gas bridge between the two fragments; (iii) a central primary configuration, characterized by a rotationally supported solution surrounded by spiral arms; (iv) a filament configuration, characterized by a thin and dense longitudinal collapsed structure without fragments present; (v) a binary configuration, characterized by two fragments, so that they are orbiting one about the other.

All of these configurations have already been observed before in the literature; in the next section we describe how these configurations are transformed one into another because the change in parameters of the parent gas structure.

3. Results

The main results of this paper are shown in color iso-density plots for a slice of particles around the equatorial plane of the spherical gas structure.

As we want to compare several collapse models in this paper, we use only one panel per model, which usually will correspond to the last available snapshot, and we use three panels to compose a mosaic in order to illustrate the resulting configurations obtained from a parent gas structure of total mass M_T.

It should be mentioned that the vertical and horizontal axes of the iso-density plots indicate length in terms of the sphere radius, which varies from zero to one in all the plots for the initial snapshot, irrespective of the model; therefore the Cartesian axes X and Y vary initially from -1 to 1. In order to facilitate the comparison of the results, in each mosaic at least, we use the same length scale for all the panels.

A comparison between models is still possible even at slightly different output times because most of the configurations have already entered a stable stage. Otherwise, the time evolution should be done with the sink technique introduced by Bate et al. (1995), so that the system can be evolved further in time.

---

[1]The letters on the right side of the number of the figure indicate the panel of the mosaic where the configuration is located

The panels of a mosaic have the same value of the virial parameter α_{vir} (equivalently, with the same β values of 0.1,0.3 and 0.48) for a given value of α. We observed that all the models with the highest α and β, given by 0.3 and 0.48, respectively, do not collapse but get dispersed. As we want to include only collapsing configurations, these models have been skipped and for this reason some mosaics are formed only by two panels. The last collapsing configurations have been grouped in other figures, because they are more likely to make better sense in mathematical terms, as their β values may be too high to keep physical significance in the theory of star formation.

Finally, for each model with M_T, α and β given, we build two mosaics, each corresponding to a perturbation amplitude a with values of a =0.1 and a =0.25, respectively; see Eq. 4; see Table 1.

3.1. The models with M_T= 1 $M_\odot$

The figures 1, 2, and 3 show the resulting systems obtained from the gravitational collapse of a M_T= 1 $M_\odot$ core, similar to "the standard test case". In Fig.1 all the panels show a well-defined pair of mass condensations connected by a filament. When β increases, the filament disappears so that the last collapsing configuration shown in panel 1 of Fig.25 is a well defined face-to-face configuration. By observing the axes of the panels it can be seen that the separation of the resulting fragments has significantly been increased for this last collapsing configuration.

When α is increased from 0.1 to 0.2, the pair of fragments can move one towards the other, so that an orbiting binary system is formed for lowest value of β, and for higher values of β, the configurations end with a central mass condensation surrounded by short spiral arms, as can be seen in the left and right panels of Fig.2 and also in the panel 2 of Fig.25.

In Fig.3, one can see that even for the lowest value of β, the resulting configuration is a central primary, which is rotationally supported, such that the gravitational collapse slows down.

It is interesting to observe the change in the outcome of models with the same β, but in which the α has been increased: from a face-to-face configuration type to a central primary type. This behavior was also observed by Riaz et al (2014).

When the mass perturbation is increased from a =0.1 to a =0.25, we can see in Fig.4 and in panel 4 of Fig.25 that a similar behavior is obtained to that which was seen in Fig. 1, but the binary separations are quite larger than that seen in the corresponding panels of

Fig.1.

We also noted that the number of orbiting binary systems is greatly increased, as can be seen in Figs.4 and 5; only the last collapsing configuration finishes as a central primary, as can be seen in panel 6 of Fig.25.

3.2. The models with M_T= 5 $M_\odot$

For all the values of β, we see that a pair of mass condensations connected by a very smooth filament are formed, as can be seen in Fig.7. When α is increased from 0.1 to 0.2, the mass condensations are very weak or they even disappear, while the filaments are thinner and more pronounced; see Fig. 8. For the highest value of α =0.3 considered here, we see in Fig.9 that the corresponding filaments become thinner and narrower and again a rotationally supported central primary surrounded by long spiral arms is seen as the last collapsing configuration for the highest value of β.

When the perturbation scale takes the new value of a = 0.25, the filaments almost disappear and instead a pair of mass condensations are seen located face-to-face and more pronounced than before, as one can see in Fig.10. Later, when α increases to 0.2, the mass condensations are weaker but still face-to-face, while no dense filaments are seen in Fig.11. We observe again that the binary separation is significantly increased in these runs, shown in Fig.10 and Fig.11, as compared with those of Fig.7 and Fig.8.

For the highest α =0.3 value considered here, we see in Fig.12 the appearance of weaker filaments and again the transition to a central primary.

In any run of the models with M_T= 5 $M_\odot$ we have not directly observed the formation of an orbiting binary system.

3.3. The clump models

We first notice that there is almost no difference between the configurations obtained for the clump of M_T= 50 $M_\odot$ with those obtained for the M_T= 400 $M_\odot$, as can be seen by comparing Figs.13,14,15 and 16,17, 18 with the corresponding figures of the largest mass clump. We take advantage of this similarity by using only the last collapsing configurations of the M_T= 400 $M_\odot$ clump to compare with the lower mass models of previous sections.

In Fig. 13 one can see that configurations of the face-to-face type connected by a weak filament are mainly formed for the two lower values of β. These filaments are fainter than

those observed in the M_T= 1 $M_\odot$ model shown in Fig.1 while they are very similar to those obtained for the M_T= 5 $M_\odot$ model shown in Fig.7.

In the right panel of Fig. 19 and panel 1 of Fig.27, which corresponds to a β =0.3 and β =0.7, respectively, still show the face-to-face configuration, as was the case for the two models of smaller total mass considered; see the panels 1 of Fig.25 and Fig.26.

When α takes the value of 0.2, the filament formed for a large β is fragmenting as can be seen in the right panel of Fig. 14, while the opposite case was seen for the M_T= 5 $M_\odot$ model in Fig.8; that is, the filament becomes denser and thinner while in the M_T= 5 $M_\odot$ model shown in Fig.2 there is no filament for comparison.

When β takes its highest possible value, still in the collapsing regime, the filament of the M_T= 400 $M_\odot$ model is replaced by a central primary configuration surrounded by spiral arms; see the panel 2 and 3 of Fig. 27 and the bottom left panel of Fig. 21. This behavior was also observed in the M_T= 5 $M_\odot$ models in Fig.8 and Fig.9 but was not observed in the M_T= 1 $M_\odot$ models with α =0.2 in Fig.2 nor with α =0.1 in Fig.1, although it occurred for this model with α =0.3, as can be seen in Fig.3.

When the mass perturbation is increased to a =0.25, more configurations of the face-to-face type appear connected by a tenuous bridge of gas; see Fig. 22. This behavior was also observed in the M_T= 5 $M_\odot$ model shown in Fig.10, but it must be mentioned that the binary separation is much larger in the former model than in the latter. Something similar was also observed for the M_T= 1 $M_\odot$ model, but there the filaments are more pronounced, as can be seen in Fig.4.

The runs with α =0.3 are similar for the M_T= 50 $M_\odot$ models and M_T= 5 $M_\odot$ shown in Fig. 23 and Fig.10, respectively, in which we see configurations of the face-to-face type. It should be noted that in the M_T=1 $M_\odot$ model, the configurations formed are not at all similar to the ones seen for the corresponding two models with larger parent mass, as an orbiting binary configuration is only seen in Fig.5.

For the M_T = 400 $M_\odot$ models with α =0.3, we see a well-defined filament that is transformed to a central primary configuration when β takes its highest value; see Fig. 24; this was also observed in Fig.12 for the M_T= 5 $M_\odot$ model. But again, there is no possible comparison with the configuration obtained for the M_T= 1 $M_\odot$ model shown in Fig.6, in which orbiting binaries were indeed observed even for this higher value of α.

For all the models of M_T= 50 $M_\odot$, we did not observe the formation of any orbiting binary system.

3.4. The last collapsing configuration

We measure the uppermost β values for all models except for the clump of M_T= 50 $M_\odot$, so that the parent structure is still within the collapsing regime to the left of these curves, while to the right of each curve, there is no collapse. The configurations found are shown in Figs. 25, 26 and 27.

In Fig. 28 we observe that the curve for the models with a=0.25 are always located to the right of the corresponding curve for a=0.1; this fact is easy to understand, as the mass perturbation weighs more, then the resulting fragments are more massive, so they need more rotational energy to reach the level in which the equilibrium between the centrifugal force and the gravitational force is to be overcome. When this happens, the fragments are separated indefinitely and the gas structure does not collapse.

3.5. A quantitative comparison of the resulting configurations

We measure the most important integral properties of the resulting collapse configurations: for binaries, we consider the fragment masses and the binary separations; for the central primaries, we consider the central mass and radius; for all the resulting fragments or primaries, we also calculate the values of the energy ratios α_f and β_f.

In order to calculate these properties, we proceeded as follows: we locate the highest density particle in the fragment's region; this particle is considered the center of the fragment. The binary separation is simply calculated as the distance between the centers associated with each fragment. We next find all the particles which have density above or equal to some minimum density value, given in advance as $\log_{10}(\rho_{min}/\rho_0) = 0.0$ for all the models. We finally check that these particles are also located within a given maximum radius r_{max} from the fragment's center. This set of particles allowed us to calculate the fragment integral properties, as the mass, including the α_f and β_f; see Arreaga et al. (2012).

The results obtained for the face-to-face configurations are shown in Figs.29, 30 and 31. For the central primary configurations, we report the mass of the central condensations results and their integral properties, which are shown in Figs.32 and 33.

All the fragment properties of the face-to-face and of central primary configurations have also been reported in Tables 2 and 3, respectively. The entries of these Tables are as follows. The first column shows the number of the model; the total parent mass M_T is shown in the second column; column third shows r_{max} in terms of the initial sphere radius R_0; columns 4, 5 and 6 of Table 2 show the mass of the fragments given in terms of M_T and

the binary separation in astronomical units; in the case of Table 3, the last column shows the mass of the central primary region in terms of M_T. The last columns give the values of the α_f and β_f.

4. Discussion

The mass seeds, implemented by means of the mass perturbation of Eq. 4, accrete mass slowly during the early evolution stage of all the simulations until they become a well-defined pair of mass condensations that move through a gas of particles. Shortly thereafter, when the mass condensations are massive enough, their translational motion can be slowed down or even stopped as a consequence of the dynamical friction of the surrounding gas. Then, the mass condensations appear to be face-to-face. At this time, a competition begins between their gravitational force, which favors their approach, and the centrifugal force due to the parent structure rotation, which favors their separation. Also, the mass condensations may or may not be connected by a filament, and as we have seen, these connecting filaments can be of very different types depending on the total mass of the parent structure and on the values of α and β.

For the M_T= 1 $M_\odot$ core models, a good combination of these forces occurs such that the assembled mass condensations are sufficiently massive yet the centrifugal force is strong enough for their gravitational attraction to make them approach each other, swing past each other, and finally separate to form an orbiting binary system. We have observed that the occurrence of these events is significantly increased when the mass perturbations weigh more, as the mass condensations are naturally more massive to overcome their centrifugal force more easily, while the β must still be high enough to make them swing past one another.

By contrast, when the mass condensations are too massive, they approach each other, make contact, and finally merge to form a single central primary condensation. In this case, the gravitational force between the mass condensations has too easily overcome the rotational centrifugal force.

For the M_T= 5 $M_\odot$ and M_T= 50 $M_\odot$ models, we observed that the mass condensations remain face-to-face in most of the runs, such that if β increases further, then the separation of the face-to-face configuration gets larger up to the point that the parent structure no longer collapses. However, for higher values of β, these face-to-face configurations give rise to a central primary configuration, such that for a slightly higher β, the parent structure does not collapse but instead expands outwards but with spherical symmetry.

We see in Fig.29 that the binary separation is correlated with the mass of the parent gas

structure. It seems that no correlation exists in the case of the fragment mass, as can be see in Fig.30. This missing correlation is expected on physical grounds, in fact, for the Taurus dark cloud, Myers (1983) reported a correlation between the mass of the newly formed stars and the mass of the associated dense proto-stellar cores. More recently, large proto-stellar masses were observed by Tobin at al. (2013).

A potentially interesting issue is the fact that some binary systems have a barycentre that is not at the Cartesian coordinate origin; see for instance the panels of Fig.7. A possible explanation for this fact is that the masses of the fragments of some binary systems are different; see Fig.30 and Table2. While it is true that the perturbation mass implemented in Eq.4 has axial symmetry, it should be remembered that each spherical radial shell was randomly populated by means of a Monte Carlo method; see 2.7. We think that the origin of the unequal masses of the fragments and the displacement of the barycentre can be explained by the development of an asymmetrical random mass seed, that grow over time and are manifested mainly later, in the more evolved binary systems. The fact that some binary systems show upward displacement while others downward, gives support to this explanation.

We notice that the mass fraction of the central primary configurations is similar for all the models reported in Table 3; this is so because the number of SPH particles entering into the central region is similar for all the models; therefore, the mass of the central primary configuration does not scale with the mass of the parent structure;see Fig.32.

It is clear that the values calculated for the energy ratios α_f and β_f, unfortunately depend on the values chosen for ρ_{min} and r_{max}, so that there inevitably is certain ambiguity in defining the fragment's boundaries. Despite of this, when we calculated the α_f and β_f values we observe that some binary fragments do show a clear tendency to virialize, as it can be appreciated in Fig.31. We emphasize that a similar conclusion can be drawn from the calculation of Arreaga et al. (2008), where plots of the α_f and β_f time evolution were also presented. On the contrary, for the central primaries, we do not observe any trend to approach the virial line; see Fig.33.

5. Concluding Remarks

In this paper, we have considered the gravitational collapse of several rotating spherical gas structures of very different size and mass, such that the collapse was triggered initially by means of the same azimuthal mass perturbation, whose amplitude has been allowed to take the values a =0.1 and a =0.25. For the sake of comparison between our models, we

have used the same set of values of the α and β ratios.

The range of α considered here, 0.1-0.3, was similar to that of Riaz et al (2014); this range reflects the observational fact that the temperatures of the gas structures are mostly in the range of 9-12 K; see Bergin and Tafalla (2007). The range of β considered here, 0.1,0.3 and 0.48, was initially motivated by recent observations of the virial parameters of clouds, so that the critical virial parameter is within the chosen range, as we mentioned in Sect.1.

However, we have extended this range of β in order to look for the last collapsing configurations, for which purpose the new range has been increased to values of 0.9 for the lowest α and around 0.4 for the highest α. This range of β values is wider than those considered by other authors; see for instance, Tsuribe et al. (1999), who used a maximum β of 0.3.

We have thus revisited many binary configurations already seen in other works, but here the configurations change depending on the mass of the parent structure. Based on these results, we present the following assessment of the effect of parent mass on the collapse.

The resulting configurations for panels with α =0.1 have a well-defined pair of mass condensations connected by a dense filament for the M_T= 1 $M_\odot$ model. The connecting filaments become weaker and almost disappear when the total mass increases to M_T= 5 $M_\odot$ and M_T= 50 $M_\odot$, respectively. The last collapsing configurations are of the same kind; that is, of the face-to-face type; see Sect.3.

When α =0.2, we have observed the formation of many orbiting binary configurations for the M_T= 1 $M_\odot$ model; this tendency becomes more pronounced when the mass perturbation increases from a =0.1 to a = 0.25, so that the more massive the mass condensations, the greater the probability of an orbiting binary configuration.

For the M_T= 5 $M_\odot$ model, what has been observed primarily are configurations where thin and dense filaments connect two very small mass condensations. When the mass of the parent gas structure is M_T= 50 $M_\odot$, mainly face-to-face configurations are formed, in which the mass condensations are predominant and the filaments become thicker and less dense than those seen in the previous M_T=5 $M_\odot$ model. The last collapsing configurations are of three kinds; i.e., some runs finish with a central primary (see Figs.1 and 19); other runs finish with a binary (see Figs.5, Figs.11 and 23), and finally, only one run finishes with a thin and dense filament (see Fig.8).

When α =0.3, we have seen the formation of most of the types of binary configurations discussed in this paper; i.e., some runs show a central primary, and other runs show a well-defined pair of mass condensations connected by a filament that becomes weaker as the total

parent mass increases. However, the last collapsing configurations are of the type of a central primary for all the models.

It must be emphasized that we have seen more differences between the outcomes of the M_T=1 $M_\odot$ model and those obtained from the M_T=5 $M_\odot$, M_T=50 $M_\odot$ and M_T=400 $M_\odot$ models. In addition, we have seen many similarities in the outcomes of these last two models. These observations indicate that there is a critical total mass not much larger than one solar mass, for which the mass condensations to be formed will be too massive and the centrifugal force will not be able to make them start to orbit around each other.

As we saw in Sect.4, the binary systems formed from massive gas structures can be the origin of wide binaries, in which a very large separation between the mass components can be reached for large values of β. It is interesting to mention that a high frequency of wide binaries has recently been observed in regions having very different physical properties; see Duchêne et al. (2004).

Lastly, we mentioned that the mass perturbation shown in Eq. 4 was invented to favor fragmentation of the so-called "standard isothermal test case" of M_T=1 $M_\odot$. For the results outlined in this paper and those reported in other papers, we conclude that this mass perturbation scheme works quite well for the low-mass gas structure, but needs some improvement for the higher mass case.

In order to calculate the integral properties of the some configurations, we took particles by applying selection criteria based on two parameters, a minimum density and a maximum radius, whose values were fixed in advance. Thus, one would expect slight differences in the reported results as they are definition-dependent. Nevertheless, we find that there is a clear correlation between total mass of the parent gas structure and the separation of binary fragments; we do not observe a similar correlation for the mass of the fragments.

It must be emphasized that the initial grid of spherical concentric shells, where SPH particles were randomly located on all the available radial surface of each shell, appears to be a well-suited setup for numerical simulations of binary formation as we have obtained in a natural way, that the mass of the fragments in binary configurations are not always equal one to the other.

The author thankfully acknowledge the computer resources, technical expertise and support provided by the Laboratorio Nacional de Supercómputo del Sureste de México through the grant number O-2016/047; I thank ACARUS-UNISON for the use of their computing facilities in the development of this manuscript.

REFERENCES

Arreaga-Garcia, G., Klapp, J., Sigalotti, L.G. and Gabbasov, R. 2007, ApJ, **666**, pp.290-308.

Arreaga-Garcia, G., Saucedo, J., Duarte, R. and Carmona, J. 2008, Rev. Mex. Astron. Astrophys, **44**, pp.259-284.

Arreaga-Garcia, G., and Klapp, J. 2010, Astron. Astrophys, **509**, A96.

Arreaga-Garcia, G. and Saucedo, J., 2012, Rev. Mex. Astron. Astrophys, **48**, Num. 1,pp.61-84.

Arreaga-Garcia, G., 2016, Rev. Mex. Astron. Astrophys, **52**, Num. 1,pp.1-15.

Balsara, D. 1995, J. Comput. Phys., **121**, 357.

Bate, M.R., Bonnell, I.A. and Price, N.M., 1995, MNRAS, **277**, pp. 362-376.

Bate, M.R. and Burkert, A., 1997, MNRAS, **288**, 1060.

Bate, M. R., Bonnell, I. A. and Bromm, V. 2002, MNRAS, **332**,pp. L65-L68.

Bate, M. R., Bonnell, I. A. and Bromm, V. 2003, MNRAS, **339**, pp.577-599.

Bate, M. R. and Bonnell, I. A. 2005, MNRAS, **356**, pp. 1201-1221.

Bergin, E. and Tafalla, M. 2007, Annu. Rev. Astro. Astrophys., **45**, 339

Bodenheimer, P., *Principles of star formation*, Springer-Verlag, 2011.

Bodenheimer, P., Burkert, A., Klein, R.I. and Boss, A.P., in *Protostars and Planets IV*, Eds. V.G. Mannings, A.P. Boss and S.S. Russell, University of Arizona Press, Tucson, AZ, USA.

Bodenheimer, P., Tohline, J. E. and Black, D. C., 1980, International Astronomical Union, Colloquium on Stellar Hydrodynamics, 58th, Los Alamos, N. Mex., Aug. 12-15, 1980. Space Science Reviews, vol. 27, Nov.-Dec. 1980, p. 247-252; Discussion, p. 253.

Boss, A.P., 1986, ApJ, **62**,pp. 519-552.

Boss, A.P., 1991, Nature, **351**, 298.

Boss, A.P., Fisher, R.T., Klein, R. and McKee, C.F. 2000, ApJ, **528**, 325.

Boss, A.P. and Keiser, S.A., 2013, ApJ, **764**, pp.1-13.

Boss, A. P. and Bodenheimer, P. 1979, ApJ, **234**, 289

Burkert, A. and Bodenheimer, P. 1993, MNRAS, **264**, 798.

Busquet, G., Estalella, R., Palau, A., Liu, H.B., Zhang, Q., Girart, J.M., Gregorio-Monsalvo, I., Pillai, T., Anglada, G. and Ho, P.T.P, 2016, ApJ, **819**, Issue 2, arXiv:1602.02500.

Delgado-Donate, E. J., Clarke, C. J. and Bate, M. R. 2004, MNRAS, **347**, pp.759.

Delgado-Donate, E. J., Clarke, C. J., Bate, M. R., and Hodgkin, S. T. 2004, MNRAS, **351**, pp. 617.

Duchêne, G., Bouvier, J., Bontemps, S., André, P. and Motte, F. 2004, Astron. Astrophys, **427**, 651.

Goodwin, S. P., Kroupa, P., Goodman, A. and Burkert, A. 2007, in Protostars and Planets V, ed. B. Reipurth, D. Jewitt, and K. Keil (Tucson: Univ. Arizona Press), 133.

Hachisu, I. and Heriguchi, Y., 1984, Astron. Astrophys,**140**,259.

Hachisu, I. and Heriguchi, Y., 1985, Astron. Astrophys, **143**,355.

Hennebelle, P., Whitworth, A. P., Cha, S.-H. and Goodwin, S. P. 2004, MNRAS, **348**, 687.

Hennebelle, P. and Teyssier, R., 2008, A&A, **477**, pp.25-34.

Hunter, C., 1977, ApJ, **218**, 834.

Kauffmann, J., Pillai, T. and Goldsmith, P.F.,2013, ApJ, **779**, Issue 2,pp.14.

Kitsionas, S. and Whitworth, A. P. 2002, MNRAS, **330**, 129.

Klein, R. I., Fisher, R. T., McKee, C. F. and Truelove, J. K. 1999, in Numerical Astrophysics 1998, ed. S. Miyama, K. Tomisaka and T. Hanawa (Dordrecht: Kluwer), 131.

Larson, R.B.,1969, MNRAS, **145**, 271.

Liu, H.B., Galvan-Madrid, R., Jimenez-Serra, I., Román-Zuñiga,C., Zhang, Q., Li, Z. and Chen, H-R., 2015, ApJ, **804**, Issue 1, Article id 37.arXiv:1505.04255.

Machida, N.M., 2008, ApJ, **682**, pp.L1-L4.

Machida, N.M., Tomisaka, K., Matsumoto, T. and Inutsuka, S., 2008, ApJ, **677**, pp.327-343.

Matsumoto, T. and Hanawa, T. 2003, ApJ, **595**, 913.

Myers, P. C., *Fragmentation of Molecular Cores and Star Formation*, ed. E. Falgarone, F. Boulanger and G. Duvert (Dordrecht, Kluwer), 1983, pp.221.

Miyama, S.M., Hayashi, C. and Narita, S., 1984, ApJ, **279**, 621.

Monaghan, J.J. and Gingold, R.A. 1983, J. Comput. Phys., **52**, 374

Palau, A., Estallela, R., Girart, J.M., 2014, ApJ, **785**, 42.

Palau, A., Ballesteros-Paredes, J., Vazquez-Semanedi, E., Sanchez-Monge, A., Estallela, R., Fall, S.M., Zapata, L.A., Camacho, V. Gomez, L. Naranjo-Romero, R., Busquet, G. and Fontani, F., 2015, MNRAS, **453**, Issue 4, pp.3785-3797.

Penston, M.V.,1969, MNRAS, **144**, 425.

Price, D.J. and Bate, M.R., 2007, ASTROPHYS SPACE SCI., **311**, pp.75-80.

Riaz, R., Farooqui, S.Z., and Vanaverbeke, S., 2014, MNRAS, **444**, Issue 2, pp.1189-1204.

Rozyczka, M., Tscharnuter, M. and Yorke, H.W., 1980, Astronomy and Astrophysics, **81**, pp.207.

Shu, F.H.,1977, ApJ, **214**, 488.

Springel, V., Yoshida N. and White S. D. M., 2001, New Astronomy, 6, 79.

Springel, V. 2005, MNRAS, **364**, 1105.

Stahler, S.W. and Palla, F., *The formation of stars*, Wiley-Vch, 2004.

Sterzik, M.F., Durisen, R.H. and Zinnecker, H., Astron. Astrophys, **411**, Num. 2, 2003, pp. 91-97.

Tobin, J.J, Chandler, C., Wilner, D.J., Looney, L.W.,Loinard, L., Chiang, H-F., Hartmann, L., Calvet, N., D'Alessio, P., Bourke, T.L. and Kwon, W., 2013, ApJ, **779**, Issue 2.

Tohline, J.E., 1981, ApJ, **248**, pp.717.

Tohline, J.E., 2002, Annu. Rev. Astro. Astrophys, **40**, pp.349-385.

Truelove, J.K., Klein, R.I., McKee, C.F., Holliman, J.H., Howell, L.H. and Greenough, J.A., 1997, ApJ, **489**, L179.

Tscharnuter, W., 1975, Astronomy and Astrophysics, **39**, pp. 207.

Truelove, J. K., Klein, R. I., McKee, C. F., Holliman, J. H., Howell, L. H., Greenough, J. A. and Woods, D. T. 1998, ApJ, **495**, 821.

Tsuribe, T. and Inutsuka, S-I., 1999, ApJ, **523**, pp.L155-L158. Tsuribe, T. and Inutsuka, S-I., 1999, ApJ, **526**, pp.307-313.

Tsuribe, T., 2002, Progress of theoretical physics supplement, **147**, pp.155-180.

This preprint was prepared with the AAS LaTeX macros v5.2.

Table 1. The models and main results

Model	$M_T/M_\odot$	a	α	β	outcome	Figure
1	1	0.1	0.1	0.1	connecting filament	1 l
2	1	0.1	0.1	0.3	connecting filament	1 m
3	1	0.1	0.1	0.48	connecting filament	1 r
4	1	0.1	0.1	0.758	face-to-face	25 1
5	1	0.1	0.2	0.1	binary	2 l
6	1	0.1	0.2	0.3	connecting filament	2 m
7	1	0.1	0.2	0.48	central primary with arms	2 r
8	1	0.1	0.2	0.5344	central primary	25 2
9	1	0.1	0.3	0.1	central primary with disk	3 l
10	1	0.1	0.3	0.3	central primary with arms	3 m
11	1	0.1	0.3	0.3983	central primary	25 3
12	1	0.25	0.1	0.1	connecting thin filament	4 l
13	1	0.25	0.1	0.3	connecting filament	4 m
14	1	0.25	0.1	0.48	connecting filament	4 r
15	1	0.25	0.1	0.8871	face-to-face	25 4
16	1	0.25	0.2	0.1	binary	5 l
17	1	0.25	0.2	0.3	binary	5 m
18	1	0.25	0.2	0.48	binary	5 r
19	1	0.25	0.2	0.5411	binary	25 5
20	1	0.25	0.3	0.1	binary	6 l
21	1	0.25	0.3	0.3	binary	6 m
22	1	0.25	0.3	0.3983	central primary	25 6
23	5	0.1	0.1	0.1	connecting filament with disk	7 l
24	5	0.1	0.1	0.3	connecting filament	7 m
25	5	0.1	0.1	0.48	face-to-face	7 r
26	5	0.1	0.1	0.6118	face-to-face	26 1
27	5	0.1	0.2	0.1	thin filament	8 l
28	5	0.1	0.2	0.3	thin filament	8 m
29	5	0.1	0.2	0.48	thin filament	8 r
30	5	0.1	0.3	0.1	connecting filament	9 l
31	5	0.1	0.3	0.3	thin filament	9 m

Table 1—Continued

Model	$M_T/M_\odot$	a	α	β	outcome	Figure
32	5	0.1	0.3	0.3594	central primary with arms	26 3
33	5	0.25	0.1	0.1	face-to-face	10 l
34	5	0.25	0.1	0.3	face-to-face	10 m
35	5	0.25	0.1	0.48	face-to-face	10 r
36	5	0.25	0.1	0.6989	face-to-face	26 4
37	5	0.25	0.2	0.1	connecting filament	11 l
38	5	0.25	0.2	0.3	face-to-face	11 m
39	5	0.25	0.2	0.48	face-to-face	11 r
40	5	0.25	0.2	0.7467	face-to-face	26 5
41	5	0.25	0.3	0.1	connecting thin filament	12 l
42	5	0.25	0.3	0.3	connecting filament	12 m
43	5	0.25	0.3	0.3918	central primary with arms	26 6
44	50	0.1	0.1	0.1	connecting filament	13 l
45	50	0.1	0.1	0.3	face-to-face	13 m
46	50	0.1	0.1	0.48	face-to-face	13 r
47	50	0.1	0.2	0.1	connecting thin filament	14 l
48	50	0.1	0.2	0.3	connecting filament	14 m
49	50	0.1	0.2	0.48	thin filament	14 r
50	50	0.1	0.3	0.1	connecting filament	15 l
51	50	0.1	0.3	0.3	thin filament	15 m
52	50	0.25	0.1	0.1	face-to-face	16 l
53	50	0.25	0.1	0.3	face-to-face	16 m
54	50	0.25	0.1	0.48	face-to-face	16r
55	50	0.25	0.2	0.1	connecting filament	17 l
56	50	0.25	0.2	0.3	face-to-face	17 m
57	50	0.25	0.2	0.48	face-to-face	17 r
58	50	0.25	0.3	0.1	connecting filament	18 l
59	50	0.25	0.3	0.3	face-to-face	18 m
60	400	0.1	0.1	0.1	connecting filament with disk	19 l
61	400	0.1	0.1	0.3	connecting filament	19 m
62	400	0.1	0.1	0.48	connecting filament	19 r

Table 1—Continued

Model	$M_T/M_\odot$	a	α	β	outcome	Figure
63	400	0.1	0.1	0.7	face-to-face	27 1
64	400	0.1	0.2	0.1	filament	20 l
65	400	0.1	0.2	0.3	connecting filament	20 m
66	400	0.1	0.2	0.48	filament	20 r
67	400	0.1	0.2	0.55	central primary with arms	27 2
68	400	0.1	0.3	0.1	connecting thin filament	21 l
69	400	0.1	0.3	0.3	filament	21 m
70	400	0.1	0.3	0.38	central primary with arms	27 3
71	400	0.25	0.1	0.1	connecting filament	22 l
72	400	0.25	0.1	0.3	connecting filament with disk	22 m
73	400	0.25	0.1	0.48	face-to-face	22 r
74	400	0.25	0.1	0.81	face-to-face	27 4
75	400	0.25	0.2	0.1	connecting filament with disk	23 l
76	400	0.25	0.2	0.3	connecting weak filament	23 m
77	400	0.25	0.2	0.48	face-to-face	23 r
78	400	0.25	0.2	0.55	face-to-face	27 5
79	400	0.25	0.3	0.1	connecting filament with disk	24 l
80	400	0.25	0.3	0.3	connecting weak filament	24 m
81	400	0.25	0.3	0.385	central primary with arms	27 6

Table 2. Physical properties of fragments of the binary and face-to-face configurations.

Model	$M_T/M_\odot$	r_{max}/R_0	M_{f1}/M_T	M_{f2}/M_T	sep [au]	α_{f1}	β_{f1}	α_{f2}	β_{f2}
4	1	0.225	5.5e-02	4.9e-02	6877.1	0.11	0.28	0.12	0.22
5	1	0.02	1.4e-01	1.32e-01	133.5	0.15	0.32	0.15	0.34
6	1	0.04	8.3e-02	1.46e-02	1062.3	0.13	0.30	0.07	0.72
15	1	1.0	3.8e-02	3.4e-02	19004.2	0.15	0.24	0.19	0.13
17	1	0.04	1.3e-01	5.6e-03	1856.3	0.16	0.31	0.09	0.86
18	1	0.1	1.0e-01	1.0e-01	2720.3	0.12	0.31	0.12	0.31
19	1	0.02	5.4e-02	5.1e-02	324.5	0.17	0.30	0.16	0.30
20	1	0.015	1.3e-01	1.2e-01	333.6	0.19	0.26	0.19	0.26
21	1	0.025	9.8e-02	9.8e-02	333.8	0.17	0.29	0.17	0.29
25	5	0.1	5.0e-02	4.99e-02	3206.4	7.7	0.23	6.40	0.20
26	5	0.15	5.3e-02	5.25e-02	55284.9	0.28	0.14	0.27	0.14
33	5	0.15	2.0e-01	1.6e-01	2002.2	2.24	0.50	0.50	0.58
34	5	0.15	1.2e-01	1.2e-01	2848.5	5.18	0.30	5.10	0.31
35	5	0.15	8.4e-02	2.2e-02	5005.9	5.90	0.26	0.08	0.58
36	5	0.15	5.36e-02	5.29e-02	86903.3	0.14	0.23	0.07	0.22
38	5	0.1	8.3e-02	4.96e-02	2502.3	5.6	0.24	0.12	0.47
39	5	0.1	5.7e-02	1.04e-02	5005.6	14.4	0.24	0.16	0.6
40	5	0.15	4.8e-02	4.8e-02	99934.4	0.40	0.20	0.17	0.22
45	50	0.062	4.77e-02	5.09e-02	37642.66	0.05	0.29	0.06	0.36
46	50	0.125	6.74e-02	5.35e-02	55592.61	0.10	0.21	0.06	0.30
52	50	0.0625	8.19e-02	7.87e-02	33227.5	0.03	0.45	0.02	0.45
53	50	0.1	7.69e-02	7.41e-02	53690.4	0.05	0.31	0.04	0.28
54	50	0.125	6.91e-02	6.66e-02	77490.5	0.08	0.28	0.05	0.23
56	50	0.05	4.63e-02	4.38e-02	40819.7	0.17	0.26	0.07	0.26
57	50	0.070	4.35e-02	4.05e-02	61478.6	0.14	0.28	0.11	0.21
59	50	0.065	6.46e-02	6.30e-02	21099.1	0.14	0.26	0.12	0.24
63	400	0.25	1.28e-02	7.17e-05	308823.5	0.13	0.04	0.15	0.35
73	400	0.4	2.05e-01	2.06e-01	259714.3	0.2	0.2	0.15	0.23
74	400	0.5	6.8e-02	6.8e-02	627298.3	0.45	0.068	0.29	0.18
77	400	0.1	8.78e-02	8.65e-02	205888.0	0.15	0.23	0.14	0.22
78	400	0.085	1.2e-02	4.1e-03	124480.4	0.17	0.03	0.23	0.23

Table 2—Continued

Model	$M_T/M_\odot$	r_{max}/R_0	M_{f1}/M_T	M_{f2}/M_T	sep [au]	α_{f1}	β_{f1}	α_{f2}	β_{f2}

Table 3. Physical properties of the fragment of the central primary configurations.

Model	$M_T/M_\odot$	r_{max}/R_0	M_F/M_T	α_F	β_F
8	1	0.03	4.6e-02	0.18	0.20
9	1	0.01	1.0e-01	0.22	0.18
10	1	0.02	7.8e-02	0.17	0.22
11	1	0.035	5.37e-02	0.18	0.21
22	1	0.015	1.14e-01	0.16	0.31
32	5	0.015	2.15e-02	0.15	0.26
43	5	0.02	2.13e-02	0.19	0.24
67	400	0.008	9.77e-03	0.13	0.27
70	400	0.005	1.20e-02	0.18	0.23
81	400	0.01	1.82e-02	0.18	0.27

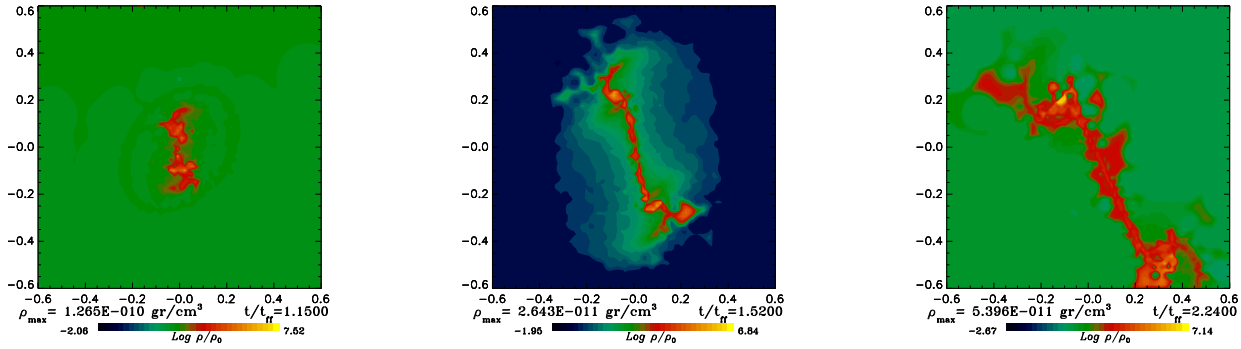

Fig. 1.— Core models with M_T= 1 $M_\odot$, a =0.1 and α =0.1; the corresponding β are (left) 0.1 (middle) 0.3 (right) 0.48.

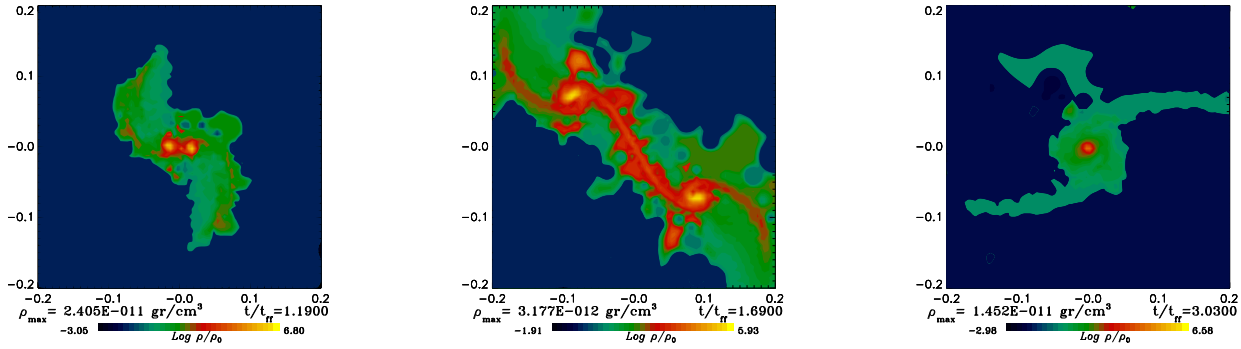

Fig. 2.— Core models with M_T= 1 $M_\odot$, a =0.1 and α =0.2; the corresponding β are (left) 0.1 (middle) 0.3 (right) 0.48.

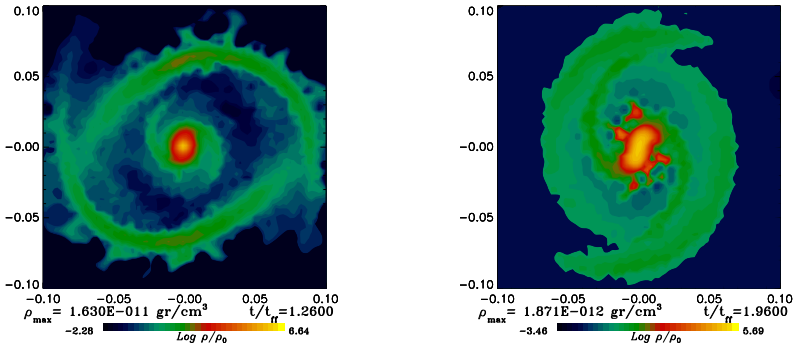

Fig. 3.— Core models with M_T= 1 $M_\odot$, a =0.1 and α =0.3; the corresponding β are (left) 0.1 (right) 0.3.

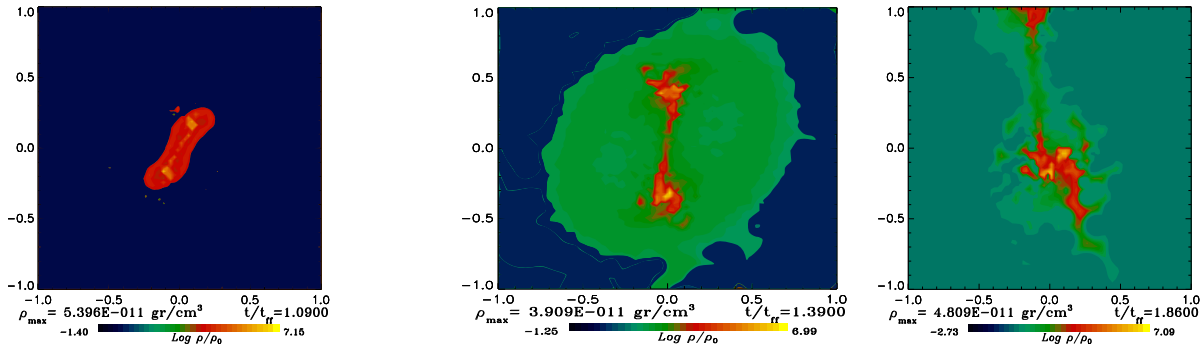

Fig. 4.— Core models with M_T= 1 $M_\odot$, a =0.25 and α =0.1; the corresponding β are (left) 0.1 (middle) 0.3 (right) 0.48.

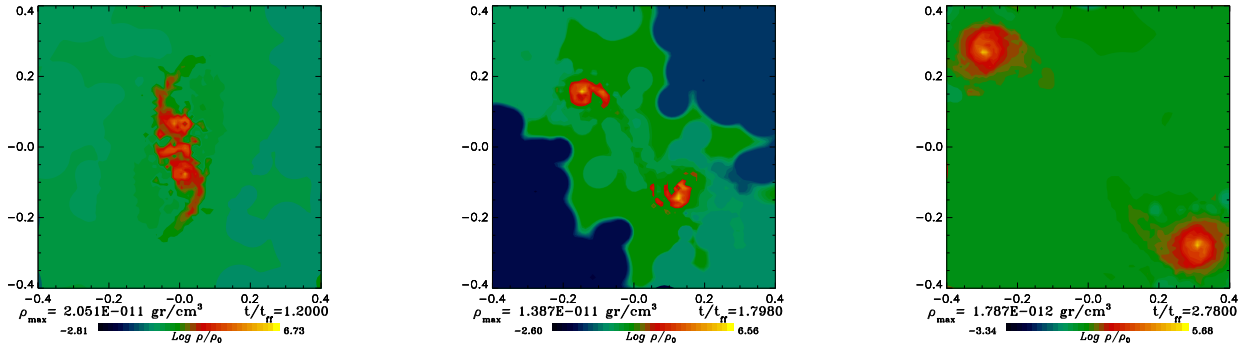

Fig. 5.— Core models with M_T=1 $M_\odot$, a =0.25 and α =0.2; the corresponding β are (left) 0.1 (middle) 0.3 (right) 0.48.

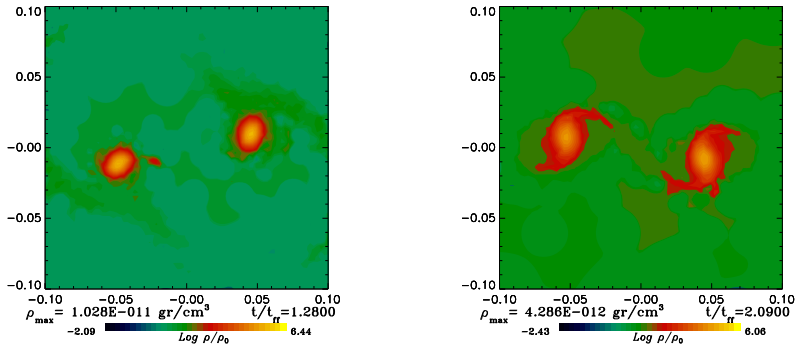

Fig. 6.— Core models with M_T=1 $M_\odot$, a =0.25 and α =0.3; the corresponding β are (left) 0.1 (right) 0.3.

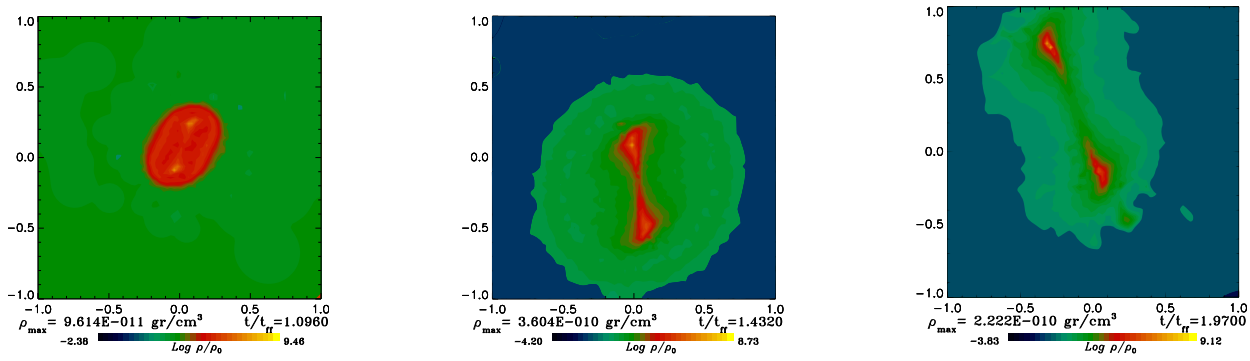

Fig. 7.— Core models with M_T=5 $M_\odot$, a =0.1 and α =0.1; the corresponding β are (left) 0.1 (middle) 0.3 (right) 0.48.

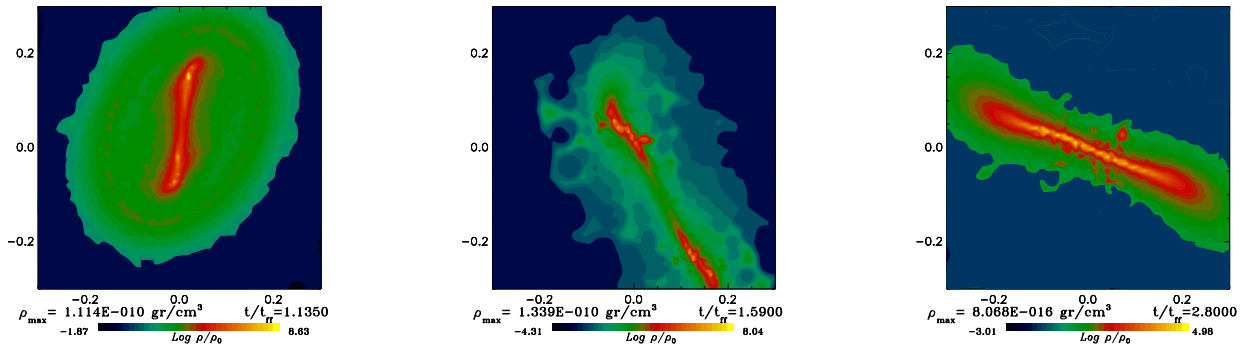

Fig. 8.— Core models with M_T= 5 $M_\odot$, a =0.1 and α =0.2; the corresponding β are (left) 0.1 (middle) 0.3 (right) 0.48. This is the last collapsing configuration; therefore, there is a missing panel in Fig.26.

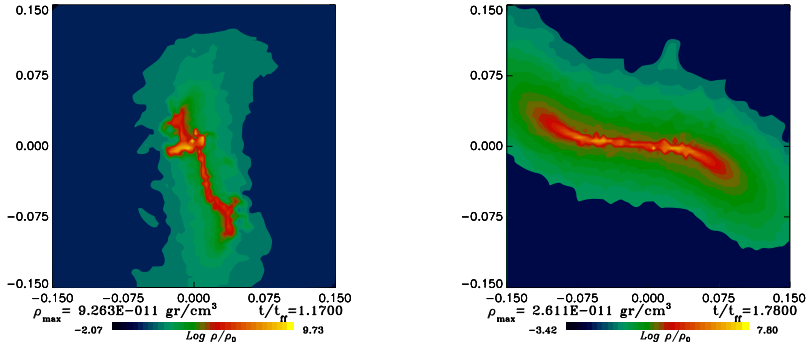

Fig. 9.— Core models with M_T= 5 $M_\odot$, a =0.1 and α =0.3; the corresponding β are (left) 0.1 (right) 0.3.

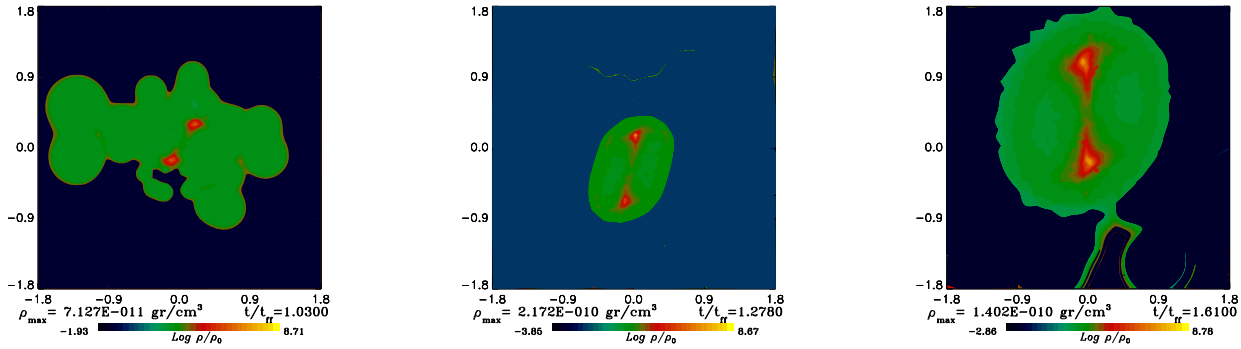

Fig. 10.— Core models with M_T=5 $M_\odot$, a =0.25 and α =0.1; the corresponding β are (left) 0.1 (middle) 0.3 (right) 0.48.

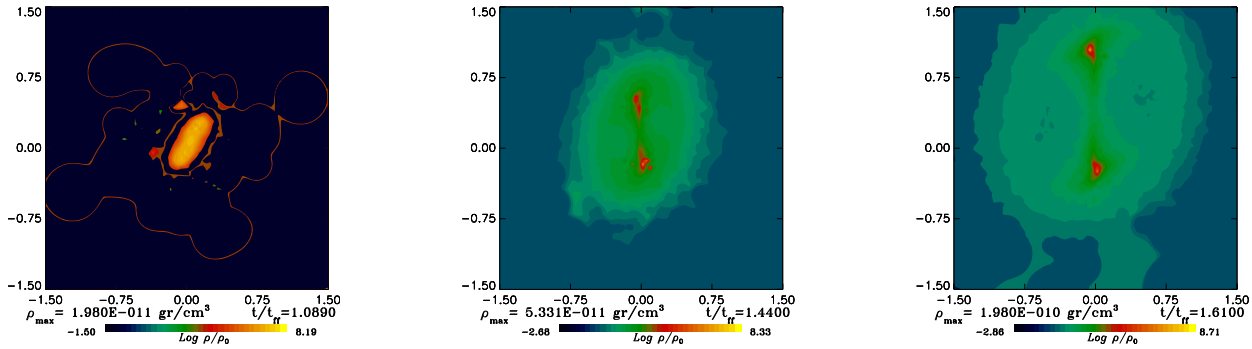

Fig. 11.— Core models with M_T= 5 $M_\odot$, a =0.25 and α =0.2; the corresponding β are (left) 0.1 (middle) 0.3 (right) 0.48.

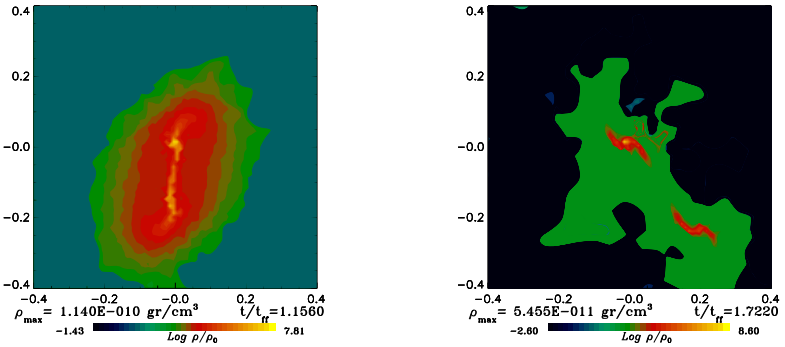

Fig. 12.— Core models with M_T= 5 $M_\odot$, a =0.25 and α =0.3; the corresponding β are (top left) 0.1 (top right) 0.3.

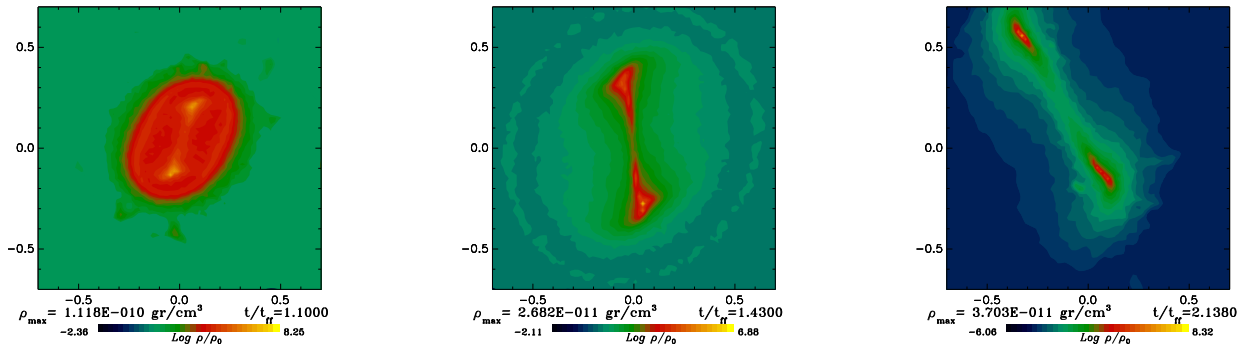

Fig. 13.— Core models with M_T=50 $M_\odot$, a =0.1 and α =0.1; the corresponding β are (left) 0.1 (middle) 0.3 (right) 0.48.

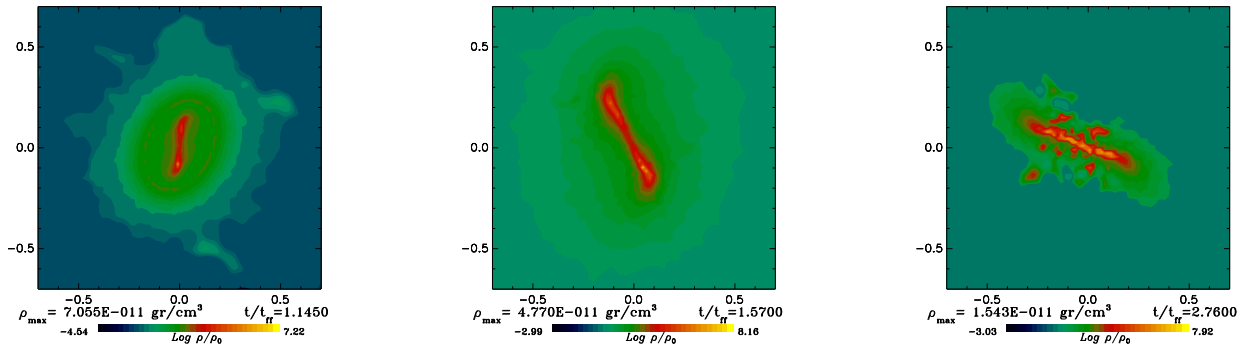

Fig. 14.— Core models with M_T=50 $M_\odot$, a =0.1 and α =0.2; the corresponding β are (left) 0.1 (middle) 0.3 (right) 0.48.

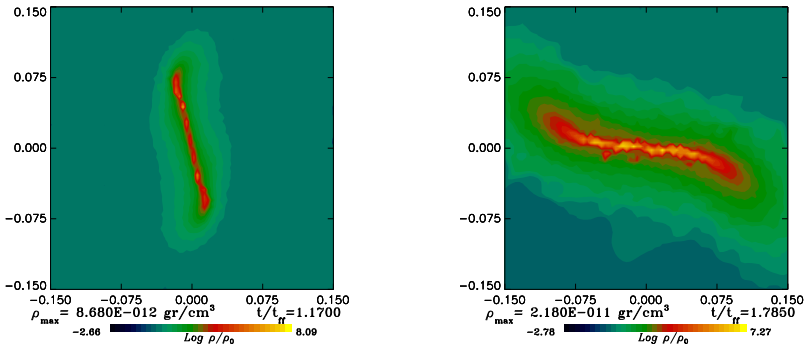

Fig. 15.— Core models with M_T=50 $M_\odot$, a =0.1 and α =0.3; the corresponding β are (left) 0.1 (middle) 0.3.

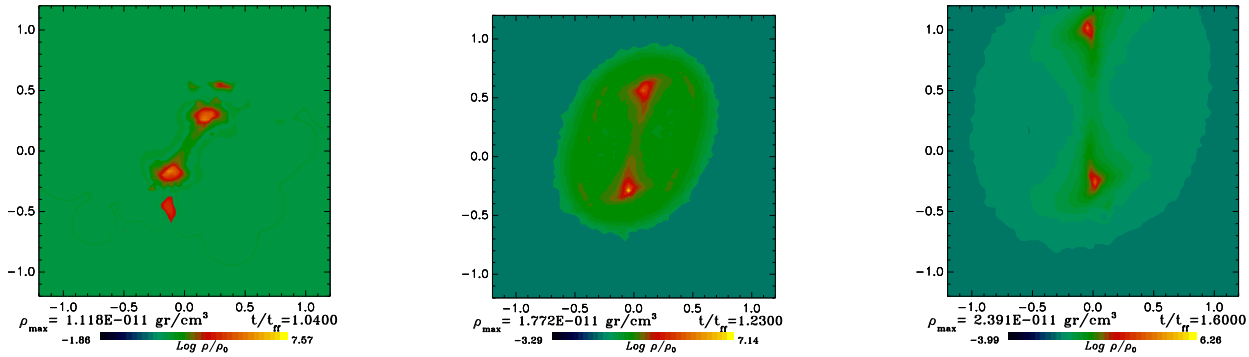

Fig. 16.— Core models with M_T=50 $M_\odot$, a =0.25 and α =0.1; the corresponding β are (left) 0.1 (middle) 0.3 (right) 0.48.

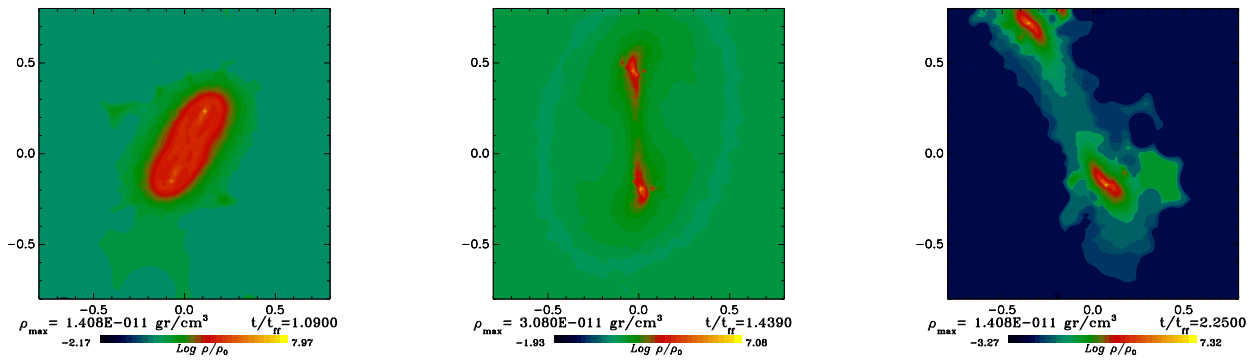

Fig. 17.— Core models with M_T=50 $M_\odot$, a =0.25 and α =0.2; the corresponding β are (left) 0.1 (middle) 0.3 (right) 0.48.

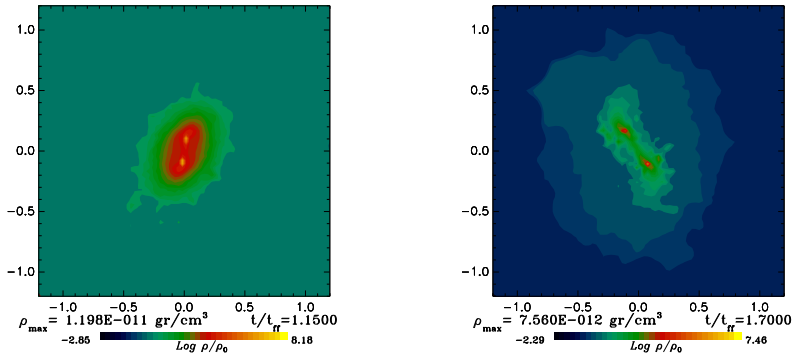

Fig. 18.— Core models with M_T=50 $M_\odot$, a =0.25 and α =0.3; the corresponding β are (left) 0.1 (middle) 0.3.

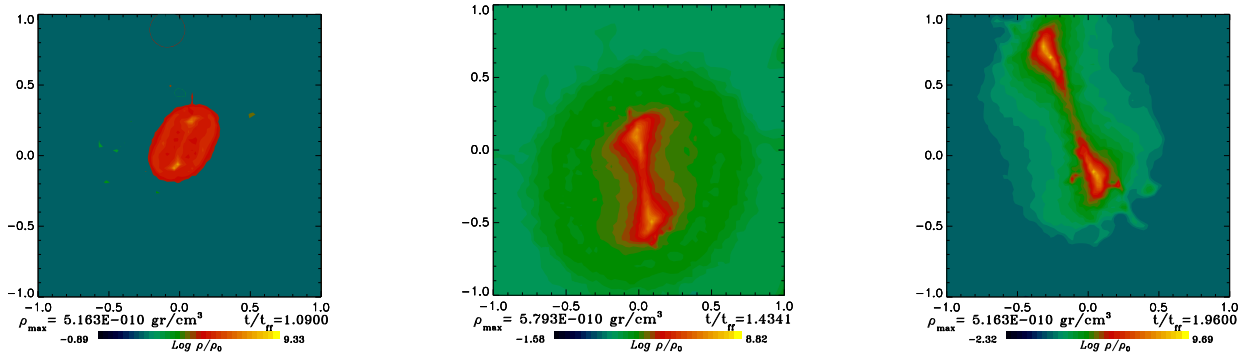

Fig. 19.— Clump models with M_T 400 $M_\odot$, a =0.1 and α =0.1; the corresponding β are (left) 0.1 (middle) 0.3 (right) 0.48.

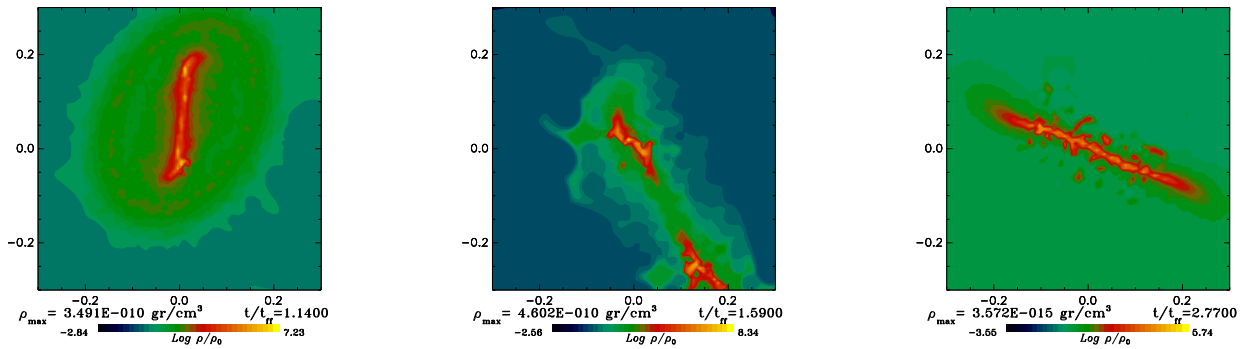

Fig. 20.— Clump models with M_T= 400 $M_\odot$, a =0.1 and α =0.2; the corresponding β are (left) 0.1 (middle) 0.3 (right) 0.48.

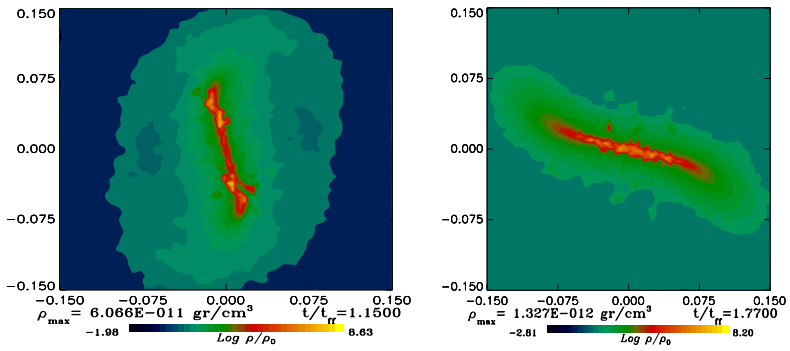

Fig. 21.— Clump models with M_T= 400 $M_\odot$, a =0.1 and α =0.3; the corresponding β are (left) 0.1 (right) 0.3.

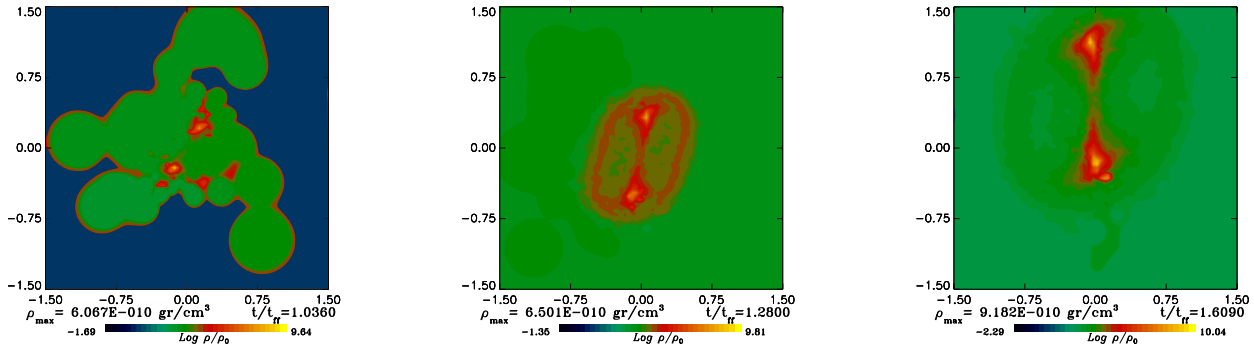

Fig. 22.— Clump models with M_T= 400 $M_\odot$, a =0.25 and α =0.1; the corresponding β are (left) 0.1 (middle) 0.3 (right) 0.48.

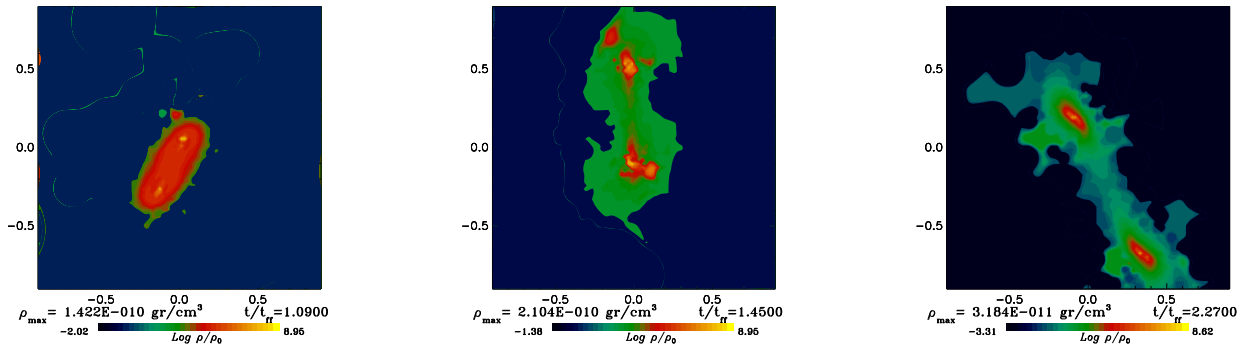

Fig. 23.— Clump models with M_T= 400 $M_\odot$, a =0.25 and α =0.2; the corresponding β are (left) 0.1 (middle) 0.3 (right) 0.48.

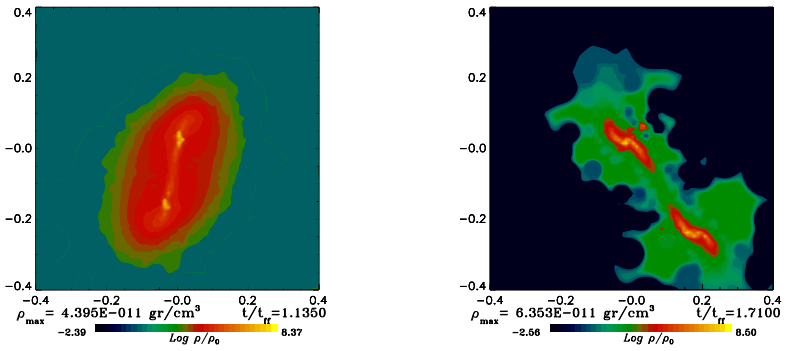

Fig. 24.— Clump models with M_T= 400 $M_\odot$, a =0.25 and α =0.3; the corresponding β are (left) 0.1 (right) 0.3.

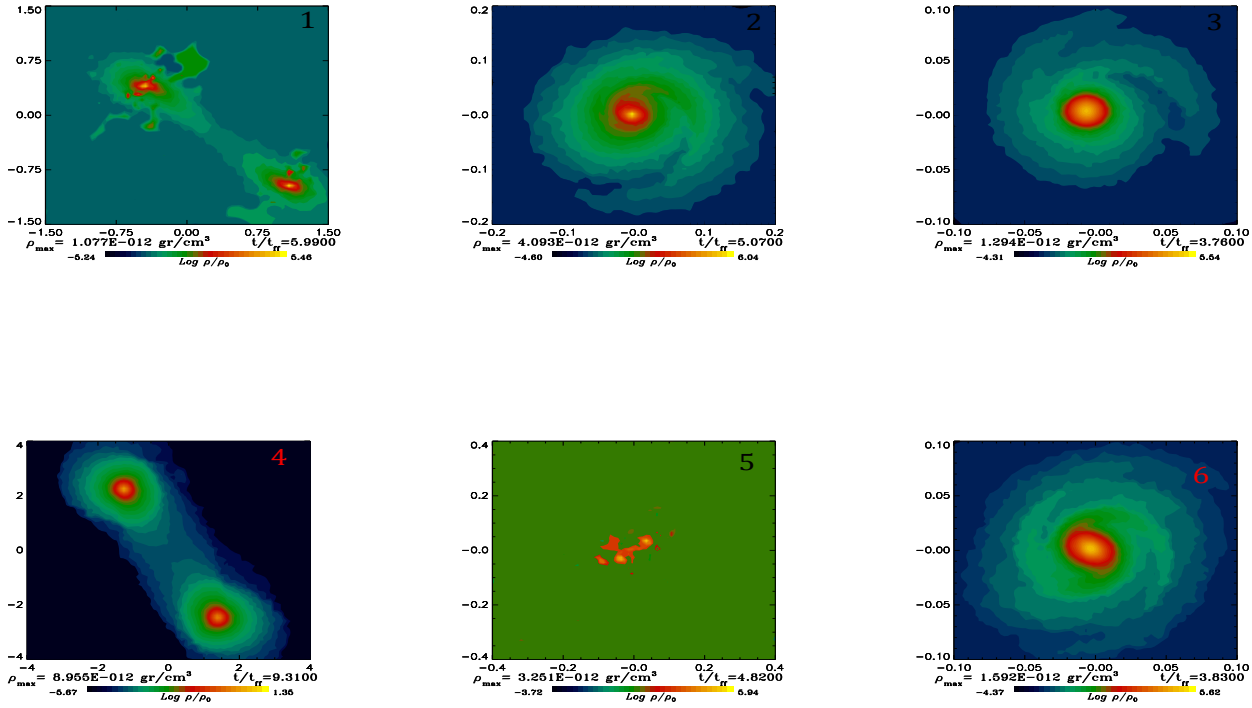

Fig. 25.— (1) M_T=1 $M_\odot$, a =0.1, α =0.1, β =0.758; (2) M_T=1 $M_\odot$, a =0.1, α =0.2, β =0.5344; (3) M_T=1 $M_\odot$, a =0.1, α =0.3, β =0.3983; (4) M_T=1 $M_\odot$, a =0.25,α =0.1, β =0.8871; (5) M_T=1 $M_\odot$, a =0.25,α =0.2, β =0.5411; (6) M_T=1 $M_\odot$, a =0.25,α =0.3, β =0.3983;

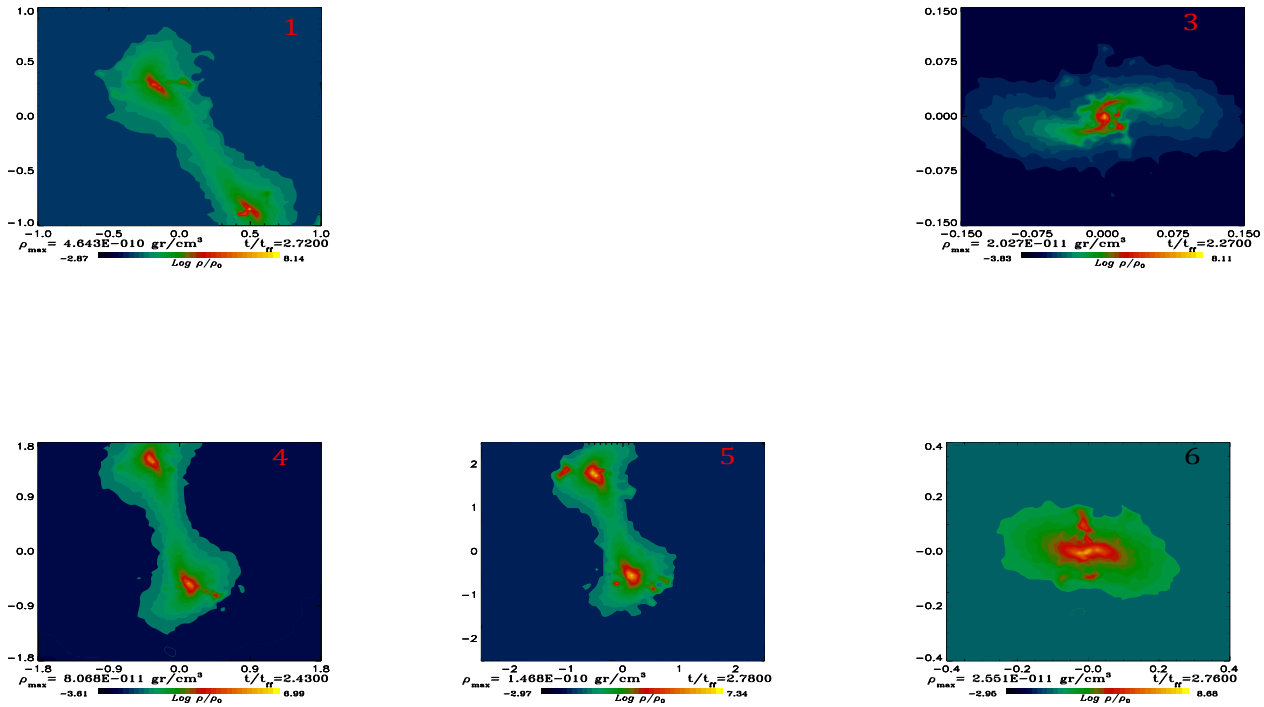

Fig. 26.— (1) M_T=5 $M_\odot$, a =0.1, α =0.1, β =0.6118; (3) M_T=5 $M_\odot$, a =0.1, α =0.3, β =0.3594; (4) M_T=5 $M_\odot$, a =0.25,α =0.1, β =0.6989; (5) M_T=5 $M_\odot$, a =0.25,α =0.2, β =0.7467; (6) M_T=5 $M_\odot$, a =0.25,α =0.3, β =0.3918;

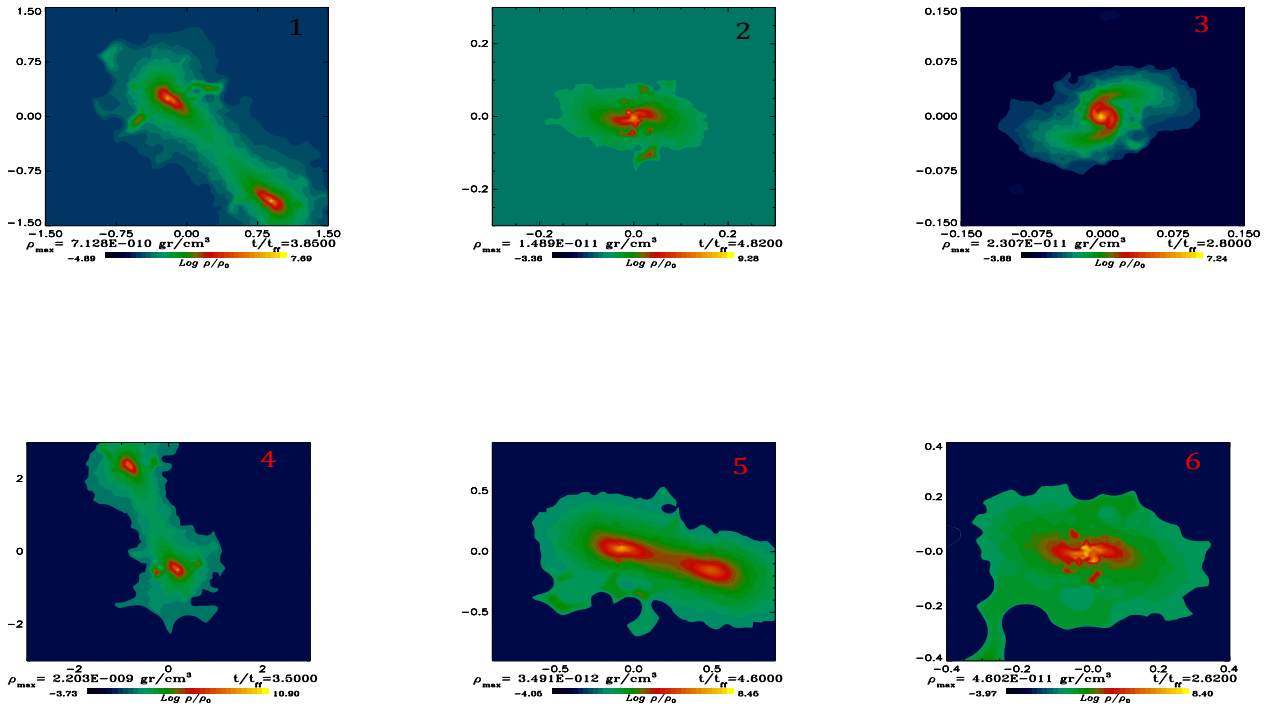

Fig. 27.— (1) M_T=400 $M_\odot$,a =0.1,α =0.1, β =0.7; (2) M_T=400 $M_\odot$,a =0.1,α =0.2, β =0.55; (3) M_T=400 $M_\odot$,a =0.1,α =0.3, β =0.38; (4) M_T=400 $M_\odot$,a =0.25,α =0.1,β =0.81; (5) M_T=400 $M_\odot$,a =0.25,α =0.2,β =0.55; (6) M_T=400 $M_\odot$,a =0.25,α =0.3,β =0.385;

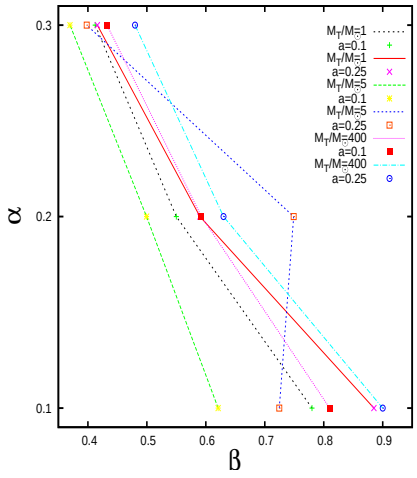

Fig. 28.— Limiting curves for all the models, so that in the region to the right of each curve, the corresponding parent gas structure does not collapse anymore.

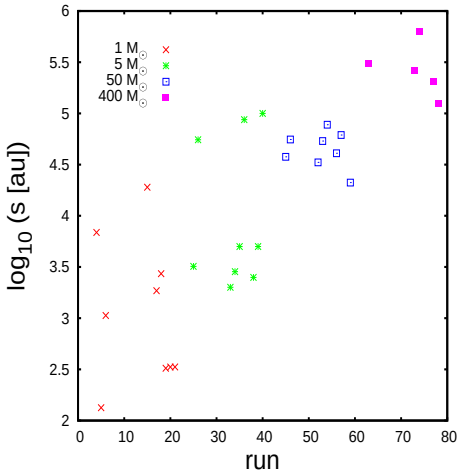

Fig. 29.— Binary separation s in terms of the run number; see Table 1.

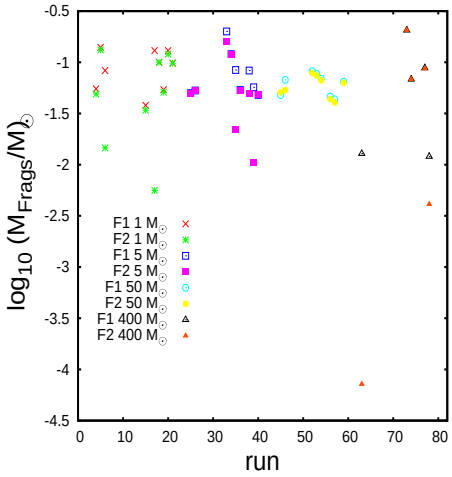

Fig. 30.— Fragment mass in terms of the run number; see Table 1.

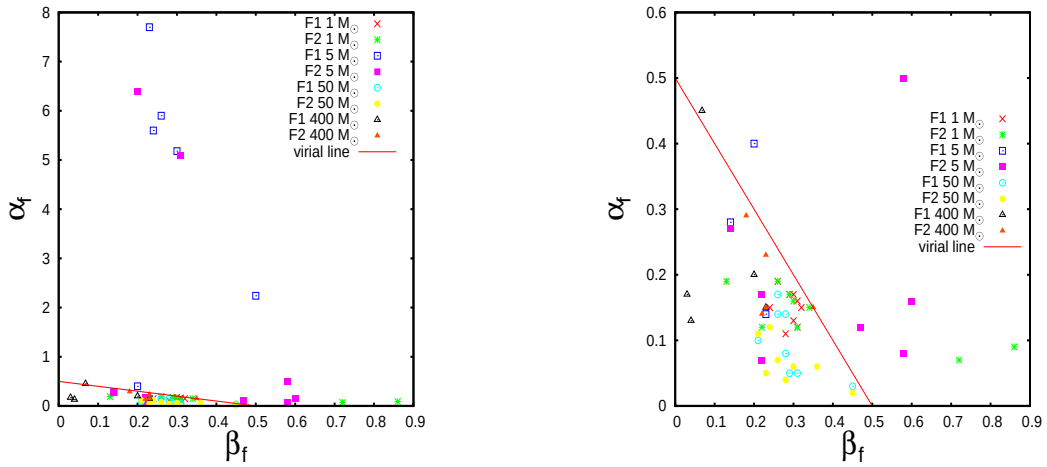

Fig. 31.— (left) Integral properties for binary fragments; (right) A zoom in of the left panel.

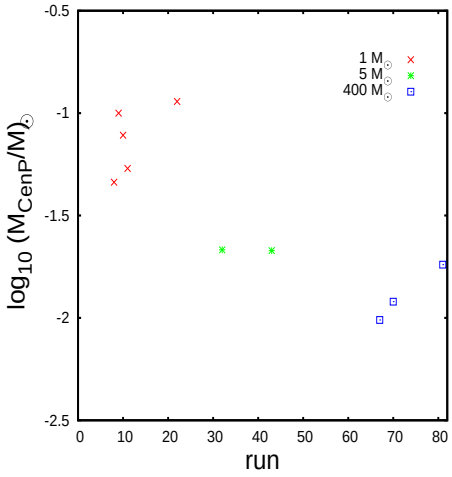

Fig. 32.— Central primary mass in terms of the run number; see Table 1.

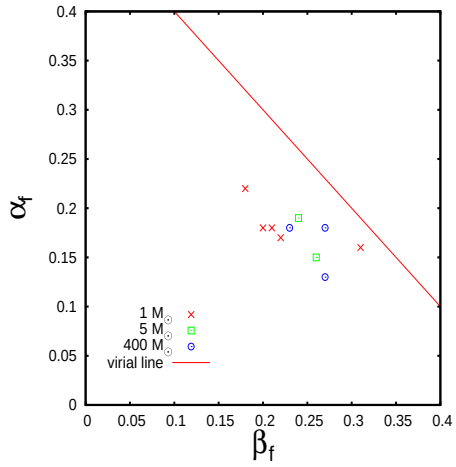

Fig. 33.— Integral properties for central primaries.